

FILE COPY

ESD-TR-75-107

LIST

XRRRI Call No. 82583

Copy No. 1 of 2 sys. ✓

2

Optics Research

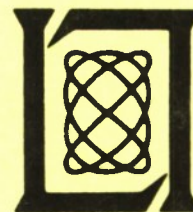
1974

Prepared for the Advanced Research Projects Agency
under Electronic Systems Division Contract F19628-73-C-0002 by

Lincoln Laboratory

MASSACHUSETTS INSTITUTE OF TECHNOLOGY

LEXINGTON, MASSACHUSETTS



Approved for public release; distribution unlimited.

ADA 010476

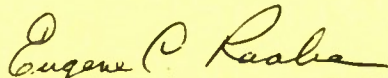
The work reported in this document was performed at Lincoln Laboratory, a center for research operated by Massachusetts Institute of Technology. This work was sponsored in part by the Advanced Research Projects Agency of the Department of Defense (ARPA Order 600) under Contract F19628-73-C-0002. Where noted, research sponsored by the Environmental Protection Agency and National Science Foundation is included.

This report may be reproduced to satisfy needs of U.S. Government agencies.

The views and conclusions contained in this document are those of the contractor and should not be interpreted as necessarily representing the official policies, either expressed or implied, of the Defense Advanced Research Projects Agency of the United States Government.

This technical report has been reviewed and is approved for publication.

FOR THE COMMANDER



Eugene C. Raabe, Lt. Col., USAF
Chief, ESD Lincoln Laboratory Project Office

Non-Lincoln Recipients

PLEASE DO NOT RETURN

Permission is given to destroy this document
when it is no longer needed.

MASSACHUSETTS INSTITUTE OF TECHNOLOGY
LINCOLN LABORATORY

OPTICS RESEARCH

SEMIANNUAL TECHNICAL SUMMARY REPORT
TO THE
ADVANCED RESEARCH PROJECTS AGENCY

1 JULY - 31 DECEMBER 1974

ISSUED 22 APRIL 1975

Approved for public release; distribution unlimited.

LEXINGTON

MASSACHUSETTS

ABSTRACT

This report covers work of the Optics Division at Lincoln Laboratory for the period 1 July through 31 December 1974. The topics covered are laser technology and propagation and optical measurements and instrumentation.

Additional information on the optics program may be found in the ARPA/STO Program Semiannual Technical Summary Reports to the Advanced Research Projects Agency.

CONTENTS

Abstract	iii
Introduction	v
Reports on Optics Research	vii
Organization	viii
 I. LASER TECHNOLOGY AND PROPAGATION	 1
A. Propagation	1
1. Thermal Blooming of Successive Laser Pulses	1
2. Multiple-Pulse Blooming of a Focused Beam in a Uniform Wind	3
3. Laboratory Experiment on Thermal Blooming	9
B. Effects	11
1. Impulsive Loading of Targets by HF Laser Pulses	11
2. Double-Pulse Pressure and Impulse Measurements	15
3. Ballistic Pendulum for High-Power Laser Measurements	21
4. Laser Heating of Metallic Surfaces	22
5. Plasma Enhancement of Thermal Coupling to Targets	29
C. Stable CO ₂ Laser Measurements	34
 II. POLLUTION STUDIES	 37
A. Participation in the St. Louis Regional Air Pollution Study (RAPS) of the U. S. Environmental Protection Agency	37
B. Diode Laser Multi-Pollutant Ambient-Air Monitoring	39

INTRODUCTION

I. LASER TECHNOLOGY AND PROPAGATION

Experiments simulating multiple-pulse atmospheric blooming with wind and slewing were done using two 10.6- μm laser pulses propagated through a propane-seeded medium. The interpulse blooming was studied as a function of pulse energy and fractional overlap.

A multiple-pulse blooming experiment has been performed using a focused 10.6- μm laser beam in an adjustable constant velocity wind. Preliminary data indicate good agreement between the experimental data and multiple-pulse steady-state computer code calculation.

Results have been obtained in the laboratory experiment on CW thermal blooming which are consistent with theory. The peak intensity vs power has been observed with and without thermal blooming (i.e., with $\alpha = 0$ and with $\alpha \neq 0$). Then, phase corrections were added to the near-field beam and an increase in the peak intensity by a factor of 2.6 was observed.

Measurements of impulse coupling coefficients for 180-nsec HF (2.7 μm) laser pulses on aluminum targets are reported. The targets were irradiated both at atmospheric and reduced pressure. Coupling coefficients of up to 13 dyne-sec/J were observed. These short-pulse 2.7- μm measurements are compared with 1.06- μm short-pulse measurements reported in the literature.

Measurements of specific impulse distribution on targets irradiated in air with single and double high-power CO_2 laser pulses are presented. The single-pulse results show that the cylindrical blast wave model adequately describes the gross features of momentum transfer to targets in the event laser-supported detonation waves are initiated. The double-pulse results indicate that for pulses with power densities on the order of 10^8 W/cm^2 and a gain-switched leading edge spike there is no impulse coupling enhancement window.

A cavity-type ballistic pendulum is intended to be used in the diagnostics and energy measurements of high-power laser beams. An experimental pendulum was fabricated and is presently undergoing testing. The measured impulse was found to be a function of the pendulum cavity shape and dimensions.

A discussion of the theory required for determining laser surface heating rates from measured surface temperature histories is presented along with experimental measurements obtained with a long-pulse CO_2 laser irradiating a copper target. These results indicate that the transfer of energy to metallic surfaces with 10.6- μm laser irradiation can be increased if a surface plasma is generated and the laser pulse is short so as not to allow the plasma to propagate very far from the surface.

Spatially and temporally resolved measurements of plasma-enhanced thermal coupling of laser radiation to metal targets are reported. Enhancement factors of 7 to 9 were observed for aluminum and copper targets.

Several improvements have been made in the experimental system used for determining the absolute frequency of natural and isotope CO_2 lasers. These include an improved 4.3- μm detection system for the Lamb-dip stabilization, a more sensitive 10.6- μm detection system with a beat frequency range well beyond 100 GHz, and an on-line mini-computer for more rapid and accurate calculation of line parameters.

II. POLLUTION STUDIES

A diode laser system has been developed and incorporated inside a mobile van. Field tests were performed in Bedford, Massachusetts and detection sensitivity of 5 ppb (parts per billion) for atmospheric CO pollution was obtained. During July to October 1974, the mobile van was driven to St. Louis to participate in the Regional Air Pollution Studies of the U.S. Environmental Protection Agency. Ambient CO measurements were performed successfully at 3 field sites located in Missouri and Illinois.*

*This paragraph describes the work performed at Lincoln Laboratory under the sponsorship of the National Science Foundation (Research Applied to National Needs), with partial support from the U. S. Environmental Protection Agency.

REPORTS ON OPTICS RESEARCH

1 July through 31 December 1974

PUBLISHED REPORT

Journal Article

JA No.

4307	Focused Beam and Atmospheric Coherence Measurements at 10.6 μm and 0.63 μm	T. J. Gilmartin J. Z. Holtz	Appl. Opt. <u>13</u> , 1906 (August 1974), DDC AD-A002502
------	--	--------------------------------	---

* * * * *

UNPUBLISHED REPORTS

Journal Articles

JA No.

4398	Long Path Monitoring of Atmospheric Carbon Monoxide by a Tunable Laser System	R. T. Ku E. D. Hinkley J. O. Sample	Accepted by Appl. Opt.
4421	Non-Chemical HF Pulse Laser Pumped by E-Beam Sustained Discharge	R. M. Osgood D. L. Mooney	Accepted by Appl. Phys. Lett.
4435	Impulsive Loading of Targets by HF Laser Pulses	S. Marcus J. E. Lowder	Accepted by J. Appl. Phys.
4436	77° InSb Isolator for 10.6 μ Using an Optimum Carrier Concentration	W. E. Bicknell L. R. Tomasetta D. H. Bates	Accepted by IEEE J. Quantum Electron.

Meeting Speeches *

MS No.

3819	Long-Path Ambient-Air Monitoring with Tunable Diode Lasers	E. D. Hinkley R. T. Ku	Conf. on Laser Atmospheric Studies, Sendai, Japan, 3-6 September 1974
3852	Laser Spectroscopy and Detection of Atmospheric Pollutant Gases	E. D. Hinkley	High Resolution Spectroscopy Symposium, Novosibirsk, USSR, 11-13 September 1974
3881	Long-Path Ambient-Air Monitoring with Tunable Lasers	E. D. Hinkley R. T. Ku	To be published in Proc. NSF-RANN Trace Contaminants Conf., Asilomar, California, 29-31 August 1974

*Titles of Meeting Speeches are listed for information only. No copies are available for distribution.

ORGANIZATION

OPTICS DIVISION

R. H. Rediker, *Head*
L. B. Anderson, *Associate Head*
M. J. Hudson, *Assistant*
V. H. Reis, *Staff*

ADVANCED TECHNIQUES AND SYSTEMS

S. Edelberg, *Leader*

Baukus, J. P.	Hinkley, E. D.	O'Neil, R. W.
Bielinski, J. W.	Ku, R. T.	Pettingill, L. C.
Blasi, J. T.	Lencioni, D. E.	Quist, T. M.
Bradley, L. C.	Levine, J. S.	Rotstein, J.
Bushee, J. F.	Lowder, J. E.	Sample, J. O.
Dickey, D. H.	McSheehy, R. B.	Sullivan, F. M.
Ellis, R. H.	Manlief, S. K.	Thomas, M. A.
Ferdinand, A. P., Jr.	Marcus, S.	Zwicker, H. R.
Henshaw, P. D.	Nork, L. P.	

OPTO-RADAR SYSTEMS

A. B. Gschwendtner, *Leader*
P. R. Longaker, *Assistant Leader*

Bauer, J. R.	Dyjak, C. P.	Martin, J. S.
Billups, R. R.	Edwards, D. M.	Merrill, E. R.
Brownson, J. S.	Hull, R. J.	Parenti, R. R.
Clay, W. G.	Johns, T. W., II	Rosato, N. F.
Coles, R. M.	Keyes, R. J.	Stevens, R. R.
Cordova, R. J.	Kleiman, H.	Zieman, H. E.
DiMarzio, E. W.	McPhie, J. M.	

INFRARED RADAR

R. H. Kingston, *Leader*
L. J. Sullivan, *Associate Leader*
P. A. Ingwersen, *Assistant Leader*

Bates, D. H.	Holtz, J. Z.	Swezey, L. W.
Bicknell, W. E.	Malling, L. R.	Teoste, R.
Capes, R. N., Jr.	Marapoti, J. V.	Tomasetta, L. R.
Daley, J. A., Jr.	O'Donnell, R. G.	Valcourt, G. L., Jr.
Fiasconaro, J. G.	Osgood, R. M.	Ziegler, H. L.
Freed, C.	Parker, A. C.	Zimmerman, M. D.
Fulton, M. J.	Scouler, W. J.	

APPLIED RADIATION

L. C. Marquet, *Leader*
E. S. Cotton, *Assistant Leader*
D. A. Page, *Assistant Leader*

Ariel, E. D.	Johnson, F. B.	Mudgett, D. A.
Bollman, R. A.	Johnson, J. Q.	Perry, F. H.
Braman, C. E.	Johnson, R. E.	Pike, H. A.
Brennan, M. J.	Kafalas, P.	Pirroni, J. S.
Chaulk, L. W.	Kelsall, D.	Pitts, R. F.
Corbosiero, D. M.	Kilcline, C. W.	Shey, S. Y.
Finne, P. C.	Kramer, R.	Stiehl, W. A.
Fouche, D. G.	Lifsitz, J. R.	Swedberg, J. L.
Grant, P. L.	McPherson, R. D.	Therault, J. R.
Herrmann, J.	Marshall, A. P.	Vernon, H. M., Jr.
Huber, E. E.	Morency, A. J.	Weaver, L. D.

I. LASER TECHNOLOGY AND PROPAGATION

A. PROPAGATION

1. Thermal Blooming of Successive Laser Pulses

Atmospheric blooming of multiple-pulse lasers with wind and slewing was simulated by using two 10.6- μm laser pulses propagated through a propane-seeded medium. The details of the experimental arrangement and initial results have been reported previously.¹

The interpulse blooming was studied as a function of fractional overlap at the cell entrance, which simulates varying wind speed and different values of αE_p , where α is the absorption coefficient and E_p is the energy per pulse.

The primary quantitative measurements were the shift in the position and the reduction of peak energy fluence of the focused beam as measured on a 16-element linear array.

The dependences of the peak reduction and shift on distortion parameter are shown in Fig. I-1. These data were obtained by varying the energy of the first pulse with $\alpha = 1.3 \times 10^{-3} \text{ cm}^{-1}$ and at a fixed overlap (100 percent) and slew angle (6 mrad). Note that the peak energy drops and the shift increases as αE increases.

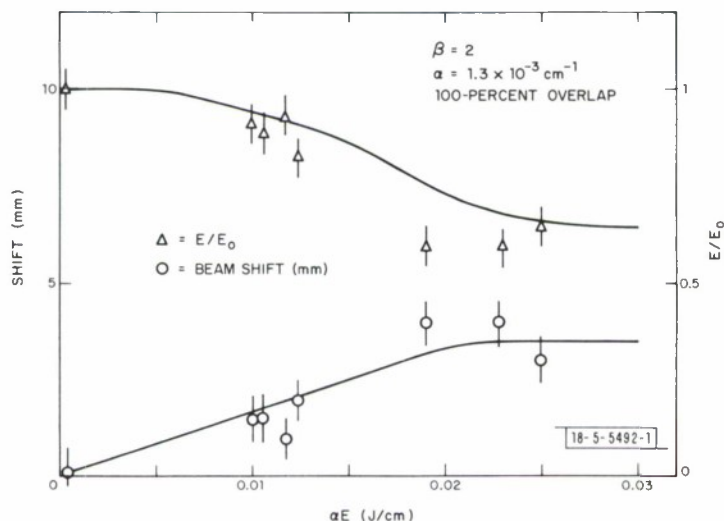


Fig. I-1. Reduction and shift of peak array energy as a function of αE for 100-percent overlap. Solid curve is theoretical prediction.

The energy shift and reduction are shown in Fig. I-2 as a function of fractional overlay at a fixed value of αE . It can be seen that increasing overlap causes increasing blooming effects.

These data were compared with predictions of the Lincoln Laboratory two-pulse computer code. The comparison was made to the calculated energy distribution appearing on a 16-element finite linear array in exact correspondence with the experimental measurement. The resulting code calculations are shown as solid lines in Figs. I-1 and -2. As can be seen, the agreement between theory and experiment is quite good.

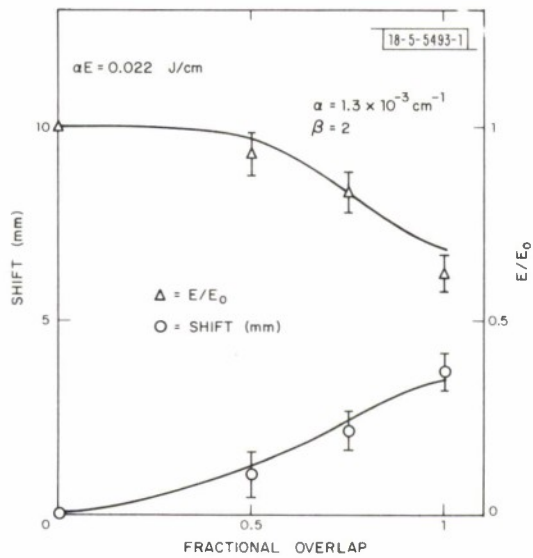
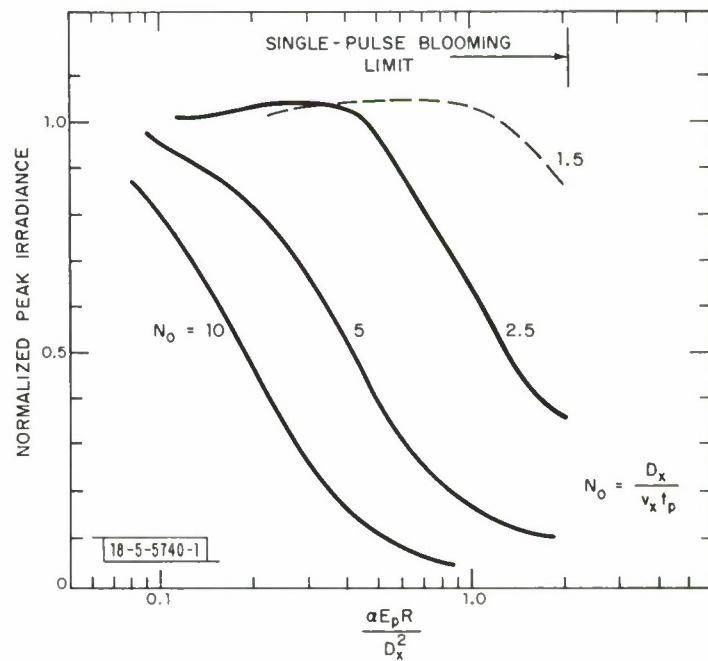


Fig. I-2. Reduction and shift of peak array energy as a function of overlap for $\alpha E = 1.3 \times 10^{-3} \text{ cm}^{-1}$. Solid curve is theoretical prediction.

Fig. I-3. Parameter space of multiple-pulse blooming experiments: normalized peak energy density plotted as a function of $N_D = \alpha E_p R / D_x^2$ for overlap numbers $N_0 = 1.5, 2.5, 5, \text{ and } 10$.



These results indicate that multiple-pulse blooming is well understood and can be predicted accurately at least for the conditions of this experiment.

R. W. O'Neil L. C. Pettingill
D. E. Lencioni J. Herrmann

2. Multiple-Pulse Blooming of a Focused Beam in a Uniform Wind

In the previous Optics Research Report, a computer code was described that computes the steady-state thermal blooming of a train of laser pulses passing through a moving medium having finite absorption when each individual pulse does not itself bloom.² In this section, we will describe the details of an experiment designed to test the accuracy and limits of this computer code. Preliminary results indicate excellent agreement between theory and experiment.

The steady-state multiple-pulse code considers a train of identical laser pulses passing through an atmosphere with specified absorption properties. The redistribution of irradiance in the n^{th} pulse in any plane along the path is calculated by propagating a non-blooming pulse through the index of refraction distribution left behind by the preceding pulses that overlap its path. In this discussion, it will be assumed that steady state is reached before the onset of convection or conduction. Then the strength of the index of refraction change is proportional to

$$\frac{\alpha E_p R}{D_x^2} \cdot \frac{D_x \nu}{v_B} \equiv N_D \cdot N_O$$

where α is the absorption coefficient in cm^{-1} , E_p is the energy per pulse, R is the propagation distance, D_x is the beam aperture width in the direction of the wind, ν is the laser repetition frequency, and v_B is the beam or wind velocity. N_O is called the overlap number, since $N_O = 5$ indicates five laser pulses occur within one flow time across the laser aperture. N_D is a measure of the strength of medium distortion caused by a single pulse. The experiment has been designed to vary α , E_p , D , and N_O , independently, at constant R .

Each of these parameters has been varied in the computer code to define an experimental parameter space. Independent calculations determine the extent of single-pulse blooming. Earlier experiments have demonstrated good agreement between experiment and theory of blooming long and short single pulses.³ The multiple-pulse parameter space is demonstrated in Fig. I-3, a plot of the peak energy density normalized to the unbloomed peak energy density reduced by linear absorption factor $e^{-\alpha L}$ where L is the length of the absorbing region.

Experiment

The following conditions were established in the experiment:

- (a) Negligible single-pulse blooming
- (b) Uniform cross wind
- (c) Maximum flux ($\alpha > 0$) less than 10^7 W/cm^2
- (d) Negligible convection or conduction
- (e) Broadband absorption
- (f) Negligible cell effects (acoustics, turbulence)

- (g) Low Fresnel number ($N_F < 10$)
- (h) Characterization of blooming by flux area redistribution and shift in peak irradiance in focal plane beyond absorption cell.

The last item requires some explanation. To avoid prohibitive single-pulse blooming with a laboratory scale laser, it was necessary to remove the depth of focus from the absorbing medium. Measurements were made in the focal plane and compared to calculation of the exact experimental conditions.

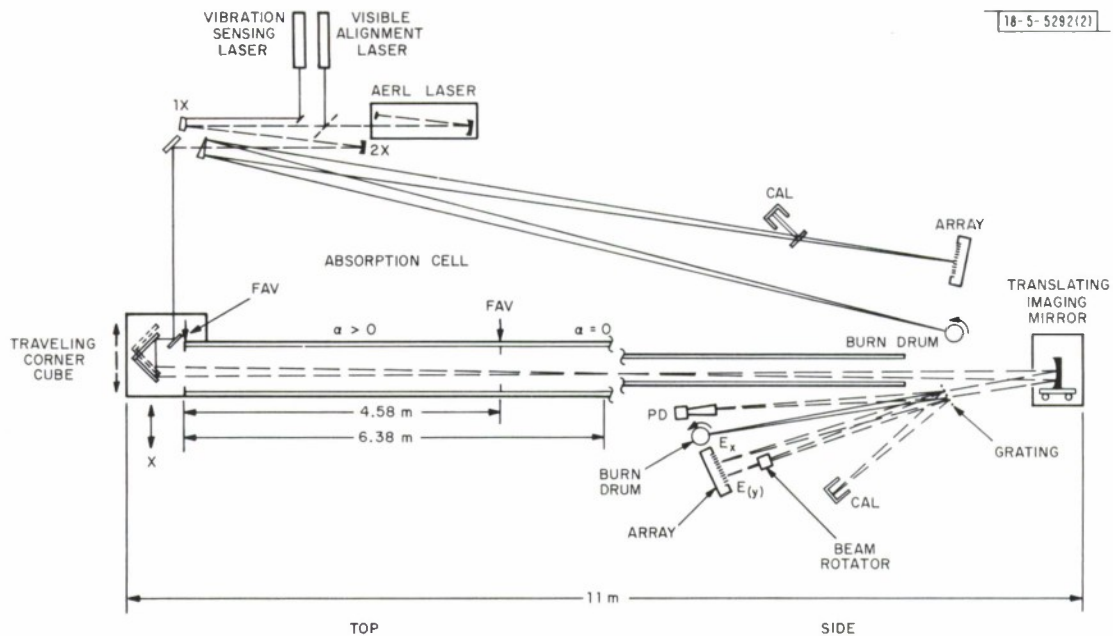


Fig. I-4. Schematic of multiple-pulse blooming experiment.

Figure I-4 is a schematic of the multiple-pulse thermal blooming experiment. The laser used in the experiments is the Avco Everett Research Laboratory (AERL) Humdinger Jr. multiple-pulse e-beam sustained CO_2 laser. For the experiments, the laser was specially modified to have a pulse length of $\sim 5 \mu\text{sec}$ (to prevent single-pulse blooming) and pulse energy of 5 to 10 J in a $2 \times 4\text{-cm}$ aperture. Pulse repetition rates were adjustable from 1 to >200 pulses per second. The laser aperture was generated by a novel off-axis unstable resonator developed by AERL to provide a good quality, reasonably uniform output irradiance distribution without the central obscuration of the more familiar on-axis unstable resonator. Because of space limitations, the absorption cell could not be located in close proximity to the laser. The laser beam was immediately passed through a 2:1 focusing beam expander to bring a converging beam to the entrance of the cell comparable in size to that leaving the laser. The beam expansion also minimizes the effects of edge diffraction on the irradiance profile during propagation to the cell. Beam scrapers were placed after the beam expander to define a rectangular beam with well-defined truncation. At the relatively low average power level of this laser, a salt beam splitter could be used to sample the laser beam before it enters the absorption cell. The absorption medium is confined to an evacuable 458-cm-long cell, 50 cm in diameter, closed by 25-cm aperture fast-acting mechanical shutters. The beam focuses 638 cm after entering the

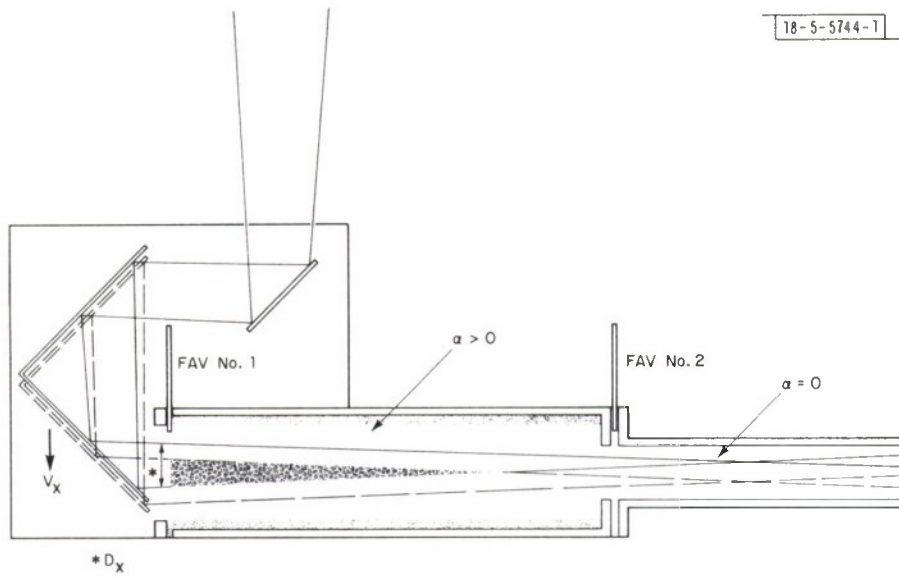
cell in a second section filled with particulate free nitrogen – a nonabsorbing gas at 10.6 μm . This feature prevents single-pulse blooming in the depth of focus and reduces the probability of dirty air breakdown to a negligible level when flux levels exceed 10^7 W/cm^2 . Propane and nitrogen are used in the absorbing section as a convenient nonsaturable broadband absorbing medium. In nitrogen, commercially obtained propane has a 10.6- μm absorption of about $10^{-4} \text{ cm}^{-1} \text{ Torr}^{-1}$. The exact cell transmittance is measured directly during the experiment.

The primary purpose of this experiment is to examine the propagation characteristics of a train of focused, partially overlapping, laser pulses as a function of overlap. To generate a uniform, reproducible wind or beam motion across the cell and measure the focal distribution of the moving beam, the optical arrangement in Fig. I-5(a) was used. A fixed beam is directed into a corner cube fabricated on a precision translation stage, as illustrated in Fig. I-5(b). Lateral movement of the corner cube a distance Δx produces a beam translation of $2\Delta x$, or a table velocity of v generates a beam velocity of $2v$. It should be noted that displacement of the corner cube does not alter the focal distance. To obtain overlap numbers of 1 to 10 for the 2-cm-wide laser beam, adjustable constant beam velocities in the range of 5 to 100 cm/sec were required. Angular stability of the moving beam through all optical elements has to be better than $\pm 150 \mu\text{rad}$. The corner cube was found to satisfy these requirements on a convenient scale.

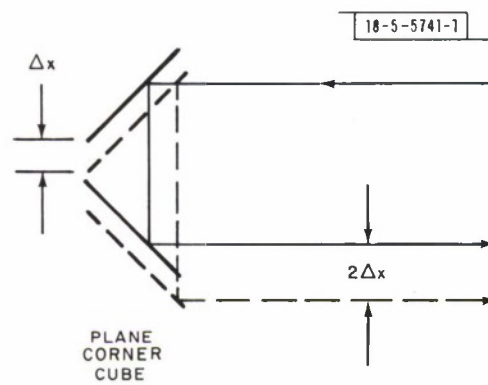
Measurement of the moving focal distributions presents two problems. The first – direct measurement of focal irradiances of $>10^7 \text{ W/cm}^2$ – is not feasible. Previous success with a focal imaging technique that permits sampling the re-imaged beam with a transmission diffraction grating was seen as the most reliable approach.³ The second problem – accurate measurement of a moving beam – was considered in this context. As indicated in the figure, an image of the moving beam can be maintained fixed in space by a mirror located to form a unit magnification image of the focal point, if the imaging mirror is translated at half the focal-spot velocity. This is seen in terms of the relative displacements in Fig. I-5(c). When an object is re-imaged at unit magnification, a displacement $2\Delta x$ in the object produces the same displacement in the image. If the mirror is moved Δx when the beam moves $2\Delta x$, the image point remains fixed in space, a practical necessity for accurate measurements.

The optical system equipment necessary to accomplish the above result consists of two movable lightweight precision optical tables. On one is mounted the corner cube consisting of two flat mirrors and on the second rests a focusing mirror. Both tables are driven by a rack and pinion gear powered by precision stepping motors deriving their commands from a common electrical pulse source. Over a total optical path from corner cube to detector of 14.5 m, image motion at the detector due to this optical system is less than $\pm 0.5 \text{ mm}$ during a table travel of 35 cm at 75 cm/sec.

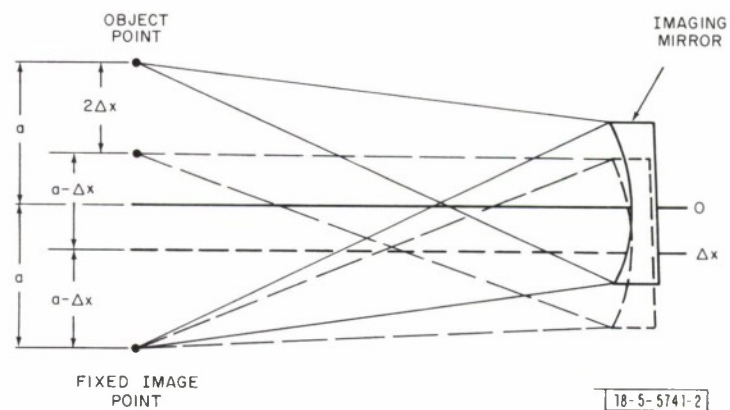
Beam diagnostics in the focal plane of the bloomed beam are performed on the monochromatic side orders of a 90-percent transmittance diffraction grating.⁴ The grating apertures, defined by 0.127-mm-diameter Be-Cu wires, are oriented parallel to beam motion and below the beam path in the re-imaging beam. The -3, 0, +3, +5, and +6 orders are used, respectively, to measure the energy transmitted through the cell, gross energy redistribution and blooming-related beam motion via burn patterns on a moving drum, power as a function of time, and the x and y one-dimensional energy distribution in the bloomed focal spot. The latter measurement is made with a pyroelectric calorimeter array with 64, $1 \times 15\text{-mm}$ elements. This array measures $\int_{-7.5 \text{ mm}}^{+7.5 \text{ mm}} E(x,y) dy = E(x)$ and analogously $E(y)$ on each pulse during a multiple-pulse run.



(a)



(b)



(c)

Fig. I-5. Optical schematic illustrating laser beam motion and stationary re-imaging techniques.

$E(y)$ is measured on the array by rotating the grating order 90° with a K-mirror. The x and y first zeros of the nearly diffraction-limited focal spot are 9.5 and 4.5 mm, respectively, and the arrays collect more than 90 percent of the unbloomed beam energy. The computer code has been programmed to calculate the measured quantities. A 32-element array of identical design measures the unbloomed beam distribution using one reflection from the salt wedge. Most of the energy in this beam is reflected into a pulse calorimeter by a high-reflection filter to measure the input energy of each pulse. The second reflection from the salt wedge is used for burn patterns on a rotating drum identical to that on the bloomed beam. The burns give a qualitative picture of shot-to-shot beam quality and a quantitative measure of input beam pointing stability. A visible beam passing through all optical elements of the system was monitored on a TV camera to determine during the experiment the total extent of beam motion due to optical element vibration. At the detector this contribution is less than $\pm 50 \mu\text{rad}$. Alignment is accomplished via a visible laser beam built into the beam expander that exactly follows the path of the $10.6\text{-}\mu\text{m}$ beam.

After calibration and background ($\alpha = 0$) data runs, the absorption cell is filled to a level of absorption for the expected pulse energy chosen from the parameter space in Fig. I-3. A laser repetition rate is chosen and the corner cube table speed is adjusted to move the laser beam at a given overlap number. A master sequencer starts a tape recorder that collects all measured signals for every pulse during a shot, turns on the laser gas flow, starts the beam moving tables, opens and, after the shot, closes the 3 mechanical shutters on the propagation cell. A microswitch on the moving tables fires the laser. Numerous timing, synchronization, and code pulses are added to the 14 channels of tape-recorded data to facilitate digitization of the analog signals. The digitized data will be processed on the IBM 370 computer.

Although the experiment is still in progress at the time of writing and the digitization is not yet complete, several sets of data have been reduced. Figure I-6 is a plot of the calculated bloomed and unbloomed $E(x)$ distributions for a set of experimental conditions. The measured

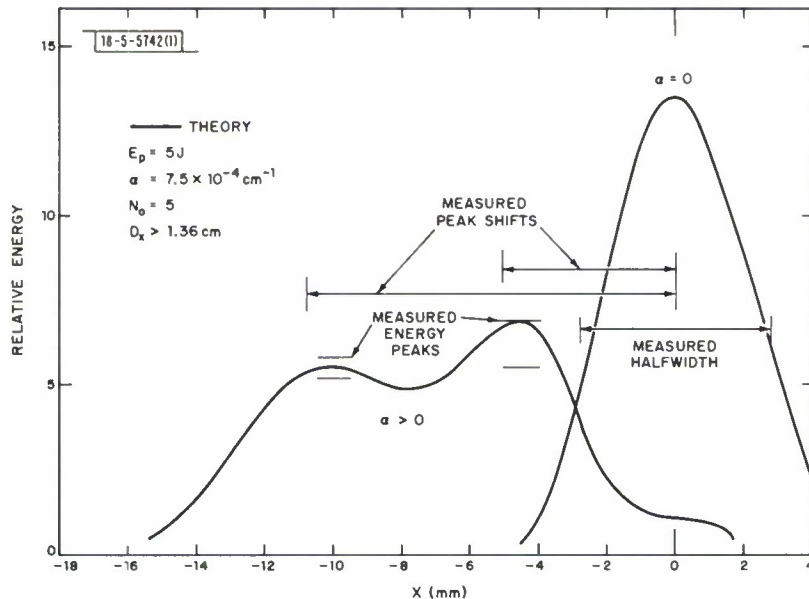


Fig. I-6. Plot of theoretically predicted bloomed and unbloomed focal distribution, $E(x)$. Fit of experimental data is indicated for measured peak energy densities and beam diffractions.

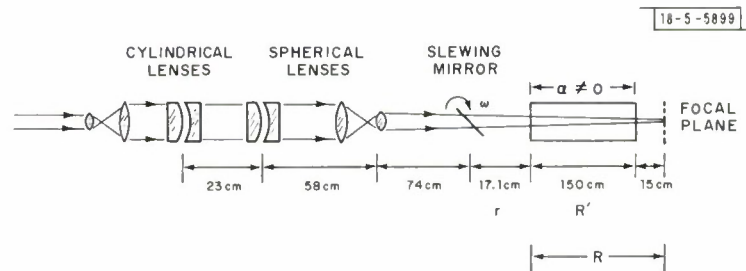


Fig. I-7. Schematic of laboratory experiment on CW thermal blooming.

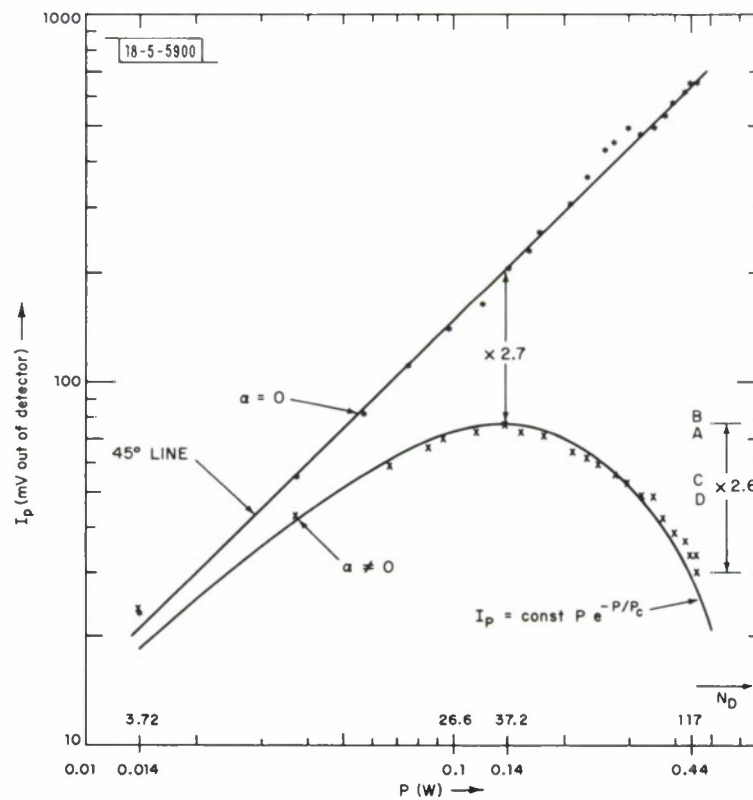


Fig. I-8. Results from laboratory experiment on thermal blooming.

reduction in energy density in the 2 peaks in the bloomed beam and their measured deflections have been indicated. With no adjustable parameter, it can be seen that the agreement is excellent.

R. W. O'Neil	L. C. Pettingill
D. H. Dickey	H. R. Zwicker
A. P. Ferdinand, Jr.	J. F. Bushee, Jr.

3. Laboratory Experiment on Thermal Blooming

Results have been obtained in the laboratory experiment on CW thermal blooming which are consistent with theory. The peak intensity vs power has been observed with and without thermal blooming (i.e., with $\alpha = 0$ and with $\alpha \neq 0$). Then, phase corrections were added to the near-field beam and an increase in the peak intensity by a factor of 2.6 was observed.

Since the results reported in the 1973:2 Optics Research Report, several improvements in the experimental setup have been made. Among these are (a) the use of CO₂ as a buffer gas instead of air so that conduction effects are less important, (b) the use of pre-mixed gas so that the absorbing gas is uniformly distributed through the cell, (c) a laser which is more stable in pointing and power output, and (d) a Gaussian laser beam.

For the results reported here, the following parameters were used (refer to Fig. I-7):

$$\begin{aligned}
 \alpha &= 2.25 \times 10^{-3} \text{ cm}^{-1} \\
 \omega &= 62.8 \text{ mrad/sec} \\
 v &= \omega r = 1.07 \text{ cm/sec} \\
 a &= 1/e \text{ radius} = 0.177 \text{ cm} \\
 b &= \text{truncation radius} = 0.330 \text{ cm} \\
 \frac{1}{\epsilon_o \rho C_p} \frac{\partial \epsilon}{\partial T} &= 1.95 \times 10^{-3} \text{ J}^{-1} \text{ cm}^3 \\
 R &= 165 \text{ cm} \\
 R' &= 150 \text{ cm} \\
 k &= 1.22 \times 10^5 \text{ cm}^{-1} \\
 \beta &= 1.6 \\
 N_S &= \frac{\omega R'}{v} = 8.77 \\
 N_A &= \alpha R' = 0.338 \\
 N_F &= \frac{k a^2}{\beta R} = 14.5 \\
 N_D &= \frac{1}{\rho C_p \epsilon_o} \frac{\partial \epsilon}{\partial T} \frac{k \alpha P R'}{\beta a v} = 266 \text{ P} \\
 0.014 &< P < 0.46 \text{ W} - \text{variable.}
 \end{aligned}$$

Phase corrections to the near-field beam were added by one pair of cylindrical lenses (cl), plus one pair of spherical lenses (sl), plus refocusing by the beam de-expander (bd). By rotating the cylindrical axes slightly with respect to one another, pure astigmatism was added to the beam. By tilting one of the spherical lenses out of the plane perpendicular to the optical axis, coma was added to the beam. Because the sl have to be separated before one of them can be tilted, these lenses also added positive focusing to the beam and, in addition, added astigmatism of the same type as the cl. Negative and positive focusing were added by the bd.

The experimental results are shown in Fig. I-8. Along the abscissa is the power entering the cell, or the distortion number ($N_D = 266 \text{ P}$). Along the ordinate is the peak intensity in the

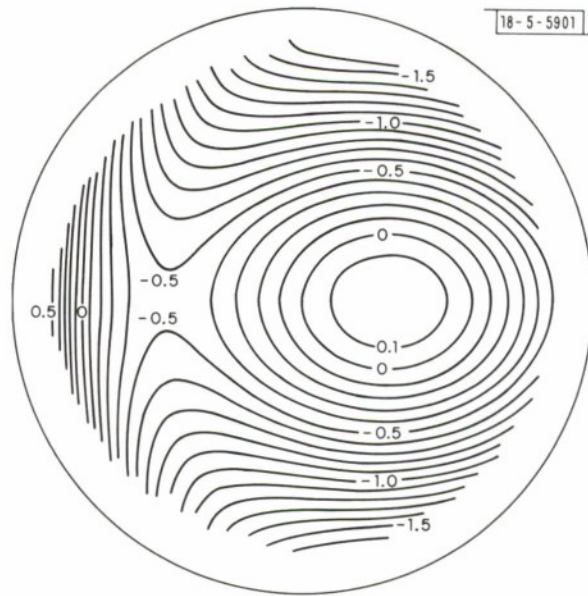


Fig.I-9. Third-order Zernike approximation to optimum phase profile predicted by propagation code. Contours in this and the following figures are labeled in units of wavelength.

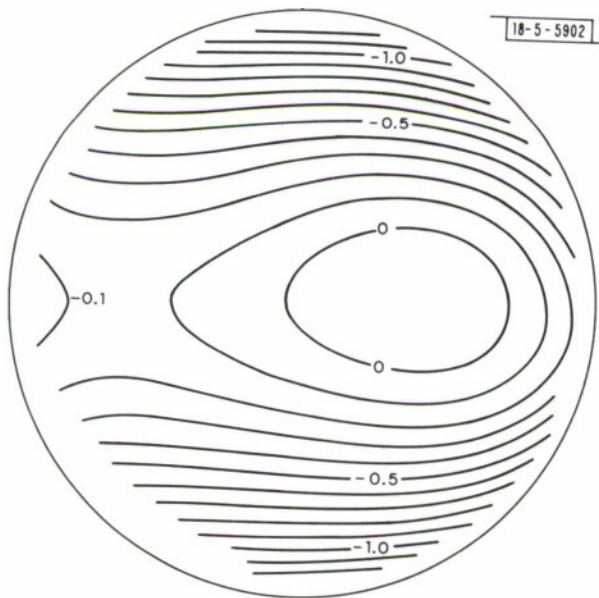


Fig.I-10. Typical phase profile added by lenses.

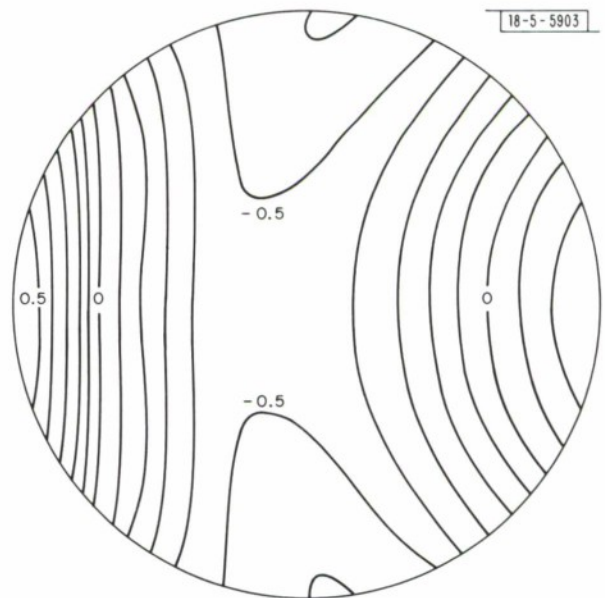


Fig.I-11. Phase profile of Fig.I-10 after some refocusing has been added.

target plane, in units of millivolts out of the detector. The asterisked points represent the I_p vs P curve when $\alpha = 0$. These points should lie on a 45° straight line, and it is evident that they nearly do. To graph the ordinate of these points, the peak voltage out of the detector was multiplied by $e^{-\alpha R^1}$ to account for the linear absorption.

The points denoted by x resulted when the absorption coefficient in the cell was increased from 0 to $2.25 \times 10^{-3} \text{ cm}^{-1}$. The curve is the theoretical curve $I_p = \text{const } P e^{-P/P_c}$, where $P_c = 0.14$ is the power at which the experimental points reach a maximum, and where the constant was chosen so that the theoretical curve would fall a factor of $1/e$ below the $\alpha = 0$ curve at $P = P_c$. It can be seen that the theoretical curve is in excellent agreement with the experimental points, even well beyond the critical power.

The additional experimental points at $P = 0.46$ (A, B, C, D) represent the peak intensity after various phase corrections have been added to the beam. Respectively, points A, B, C, and D represent the peak intensity reached with the cl, sl, and bd, the cl and bd only, the sl and bd only, and the bd only. The maximum increase came with the cl and bd, where the peak intensity was increased by a factor of 2.6 over that of the uncorrected case. Point A is not higher than point B in these preliminary experiments because the strategy in adjusting the various cl, sl, and bd lens parameters was not optimized. The optimum strategy is complex because the surface of I_p vs Astigmatism, Coma, and Refocus may have numerous peaks and valleys, so that one may end up on a local maximum instead of on the absolute maximum, and also because tilting the spherical lens adds astigmatism in addition to the desired coma.

It was difficult to get improvements by more than a factor of 2.3. Improvements by $\times 1.5$ to 2.0 occurred over a wide range of combinations of cl rotation, sl tilt, and bd refocus.

In order to compare the experimental results to those predicted by the Lincoln Laboratory propagation code, the code was run through the computer using all the laboratory parameters. A value of $P = 0.44$ was used in the code. (The experimental points in Fig. I-8 are at $P = 0.46$. At $P = 0.44$ in the experiment, an increase in I_p by a factor of 2.2 was obtained by adjusting the lenses.) The code predicted that I_p could be increased by a factor of 2.57 by adding the optimum phase profile to the beam. Figure I-9 shows the third-order Zernike approximation to the optimum phase profile. Figure I-10 shows a typical laboratory phase profile added by the lenses. This is similar to the propagation code phase profile in Fig. I-9. Figure I-11 shows the profile of Fig. I-10 after some refocusing has been added and is the actual profile used to obtain a factor of 2.2 increase in the laboratory. The code and experimental results are in reasonable agreement — both in the amount of improvement and in the type of phase profile needed to effect the improvement.

D. G. Fouche

B. EFFECTS

1. Impulsive Loading of Targets by HF Laser Pulses

Several experimenters have reported measurements of momentum transfer to targets for laser pulses of various wavelengths and pulse durations.⁵⁻⁹ We report here the first such measurements at $2.7 \mu\text{m}$. Aluminum targets were irradiated by 180-nsec pulses of up to 6 J, which were generated by an electron-beam-initiated chemical HF laser.

In our experimental arrangement, as shown in Fig. I-12, the laser beam was focused onto the target by a 4-inch-diameter, 6-inch focal-length infrared lens, which also served as an entrance window to the vacuum chamber. Such a fast lens was made necessary by the large beam

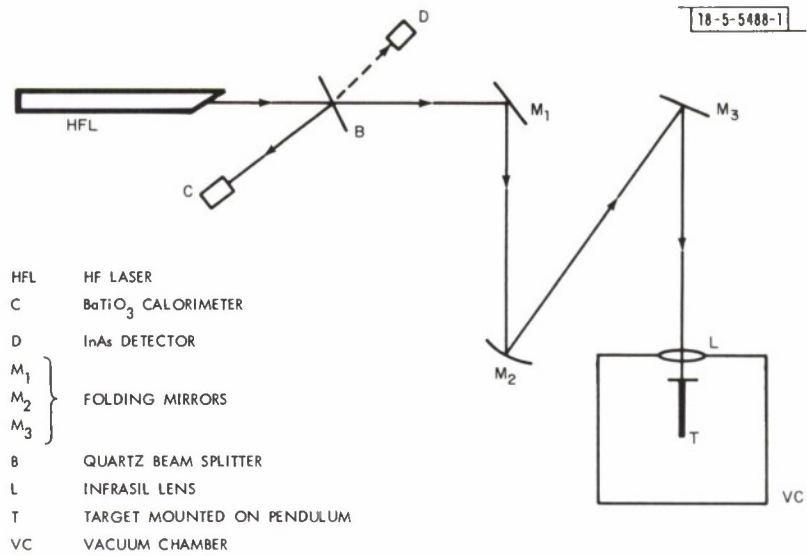


Fig.I-12. Experiment arrangement for impulse coupling measurements.

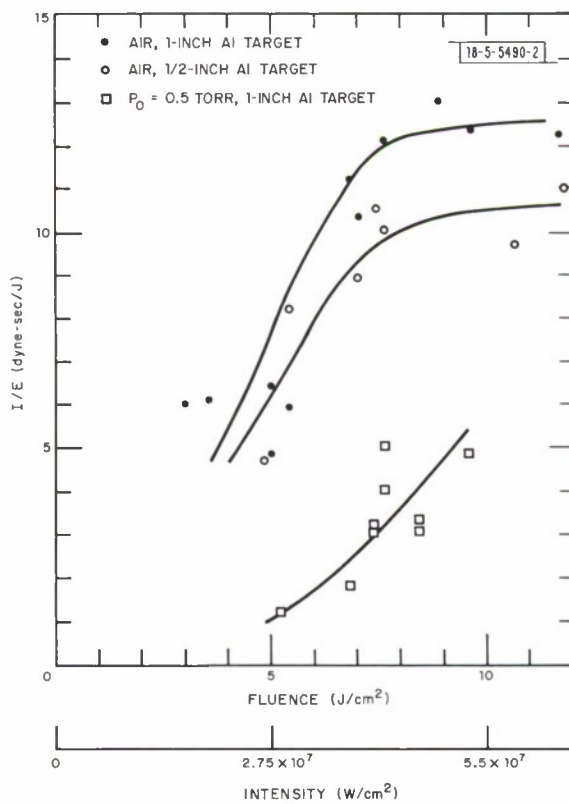


Fig.I-13. Impulse coupling coefficient vs fluence on target for 1/2- and 1-inch-diameter aluminum targets. The thickness of all targets was 0.010 inch.

divergence of our super-radiant laser. The target itself was mounted on a free-swinging pendulum (described in Ref. 9) whose displacement was monitored by a photodiode-light-source assembly. In this manner, the target momentum, which is proportional to the displacement amplitude, was recorded. A GE-125 quartz beam splitter was used to reflect a portion of the beam into a BaTiO₃ calorimeter to measure the energy of each shot. Scattered radiation from this beam splitter was intercepted by a sensitive InAs photodetector to provide a measurement of the pulse shape. The energy density profile in the focal plane was determined by measuring the blackened area on heat-sensitive paper at several levels of attenuation. By this technique, it was determined that 67 percent of the energy is contained within an area of 0.5 cm². The focal spot was somewhat "doughnut" shaped, however (\approx 25-percent dip at spot center), due to the spherical aberration of the lens.

For the data presented here, a fresh target, cleaned with Freon and alcohol, was used on each laser shot. It was noted that a second shot on a target always resulted in a reduced impulse delivery. Such a surface "cleanup" phenomenon has been observed previously and is reported in Refs. 10 and 11.

Plotted in Fig. I-13 is the observed momentum transfer per unit energy on target (I/E) vs fluence for 1/2- and 1-inch-diameter targets at atmospheric pressure, as well as for 1-inch targets with the chamber evacuated to 0.5 Torr. It is clear from this figure that at the laser energies available, significantly more impulse is delivered in air than in vacuum for a given laser pulse energy. This phenomenon is due to the lower threshold for plasma formation in ambient air⁸ and the enhanced impulse coupling over pure blowoff caused by the resulting blast wave as it expands over the surface of the target.⁹ This is also the reason the impulsive transfer is somewhat greater for the 1-inch-diameter target than for the 1/2-inch-diameter target. Open-shutter photography shows the region of plasma luminosity extends slightly beyond the edge of the 1/2-inch-diameter target for irradiation in ambient air, while for irradiation with a pressure of 0.5 Torr the luminous region is much smaller. These data show the threshold behavior for the onset of momentum transfer discussed in Ref. 9. After exceeding the threshold for plasma production (2×10^7 W/cm² in this case), the coupling coefficient increases rapidly, then becomes relatively constant above a fluence of 8 J/cm² for irradiation of targets at atmospheric pressure.

The values of I/E reported here (up to 13 dyne-sec/J) are, to our knowledge, the highest yet reported for aluminum targets in air. They are consistent, however, with extrapolation of the 1.06- μ m data of Jones and Rudder,⁷ who have measured I/E for aluminum targets in air as a function of fluence for pulse widths from 3 psec to 10 μ sec. The range of the short-pulse 1.06- μ m measurements from Jones and Rudder⁷ is indicated in Fig. I-14 by the crosshatched area. The solid symbols are the present 2.7- μ m measurements for the 1/2-inch-diameter aluminum target in air. The short-pulse (250 psec) threshold measurements from Metz⁸ are represented by the dashed line. The 1.06- μ m threshold measurements for three pulse lengths from Rudder¹² are shown as the open symbols. In general, the 2.7- and 1.06- μ m results shown in Fig. I-14 are consistent and show the power density for maximum impulse coupling in air ranges from 10^7 to 4×10^7 W/cm² as the pulse length decreases from 20 to 0.2 μ sec.

An attempt was made to correlate our low pressure results quantitatively with the model for laser-produced vaporization in a bulk material described by Ready.¹³ However, to calculate a threshold for vaporization of 2×10^7 W/cm² (our observed threshold for momentum transfer), it was necessary to postulate a surface absorptivity of nearly 100 percent. It is likely that, as

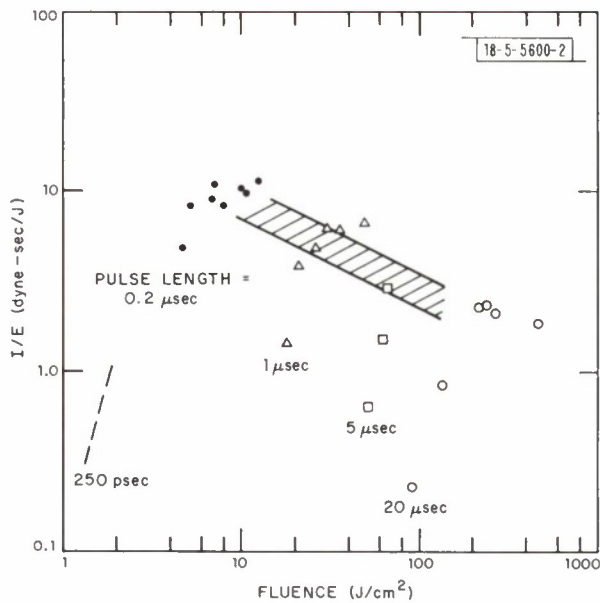


Fig.I-14. Comparison of 2.7- and 1.06- μm short-pulse coupling coefficients for aluminum targets in air. Solid symbols are present 2.7- μm measurements; open symbols are data from Ref. 12; data in crosshatched region are from Ref. 7; data represented by the dashed line are from Ref. 8.

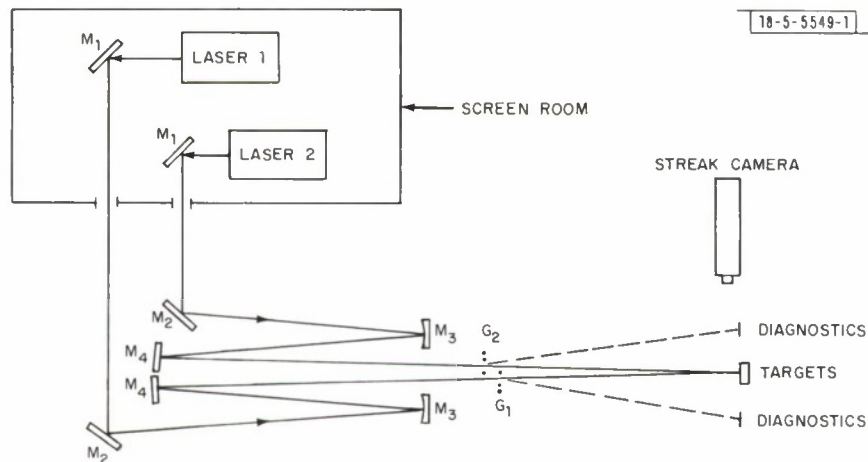


Fig.I-15. Schematic diagram of the experimental arrangement. Mirrors M_1 , M_2 , and M_4 are flats, while M_3 was either a 30- or 50-m focal-length focusing mirror. Linear wire diffraction gratings are indicated as G_1 and G_2 . The beam diagnostics included pyroelectric (BaTiO_3) calorimeters, photon drag detectors, and thermally sensitive paper.

proposed by Walters and Barnes,¹⁰ initial surface vaporization is that of thin surface laminations having poor thermal contact with the substrate. Such a local heating model, which depends on random surface defects, is consistent with our observation of surface "cleanup" and tends to explain the large scatter of our data. Under such localized heating conditions, temperatures sufficient for thermionic emission occur early in the pulse,¹⁰ resulting in increased absorption due to inverse bremsstrahlung, thus explaining our low threshold for momentum transfer. Since the absorption coefficient for inverse bremsstrahlung in the field of neutrals is proportional to the neutral number density,¹⁰ this model accounts as well for the observed lower threshold in air than at reduced pressure.

S. Marcus
J. E. Lowder
J. F. Bushee, Jr.

2. Double-Pulse Pressure and Impulse Measurements

Measurements of impulse and pressure distributions on an aluminum target irradiated with single and double pulses from the Lincoln Laboratory dual 500-J CO₂ laser system are reported. This work is the conclusion and summary of the work reported in Ref. 14, where focal-spot impulse was measured and the laser-produced plasmas were investigated via interferometry, cross-beam absorption at 10.6 μm , and high-speed streak photography. These experiments consisted of irradiating an aluminum target in ambient air with single and double pulses and measuring the impulse delivered to the focal spot and the distribution of specific impulse outside the focal spot. The single-pulse focal-spot impulse and radial specific impulse distributions outside the focal spot are compared with cylindrical blast-wave model predictions.

a. Experimental Procedure

The e-beam CO₂ lasers are capable of producing up to 500 J with a pulse duration of about 15 μsec and near-diffraction-limited beams. The laser pulse typically consists of a 300-nsec gain-switched leading edge spike followed by a 15- μsec tail. The peak power in the spike is usually a factor of 3 greater than the average power during the 15- μsec pulse. The lasers are capable of firing with a variable delay time between pulses and having their output beam focused at the same point on a target.

A schematic diagram of the optical layout is shown in Fig. I-15. The two lasers and associated electronics are contained in a screen room and the two beams are brought out through holes in the screen room wall. The laser beams are focused with 30-m focal-length mirrors (M_3 in Fig. I-15) and brought close together with the flat mirrors (M_4). The two beams are sampled with the linear wire diffraction gratings G_1 and G_2 which are adjusted at an angle relative to each other so as to separate the two sets of diffraction orders in the target plane. The beam diagnostics consisted of measurements of energy, power, and focal-spot energy distribution for each beam with pyroelectric (BaTiO₃) calorimeters, photon drag detectors, and analysis of burn patterns on thermally sensitive paper.⁴

The target for these experiments consisted of an aluminum plate with a 0.38-cm-diameter aluminum rod suspended as a pendulum¹⁵ inserted in a slightly oversize hole drilled in the plate. Three fast-response quartz pressure gauges (1- μsec response PCB gauges) were mounted in the plate in line with the pendulum with 1.27-cm center-to-center separations. The sensitive area of these pressure gauges was also about 0.38 cm in diameter.

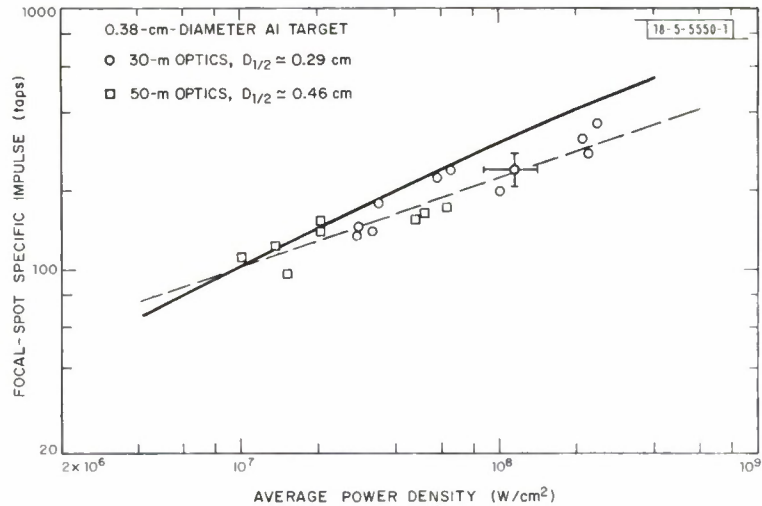


Fig. I-16. Focal-spot specific impulse as a function of average power density. The solid line was calculated with the use of Eq. (I-1) and the dashed line was fit to the data with a slope of $1/3$ and is given by $I_s \approx 0.5 (\bar{q})^{1/3}$. The error bars denote the uncertainty in the measurements.

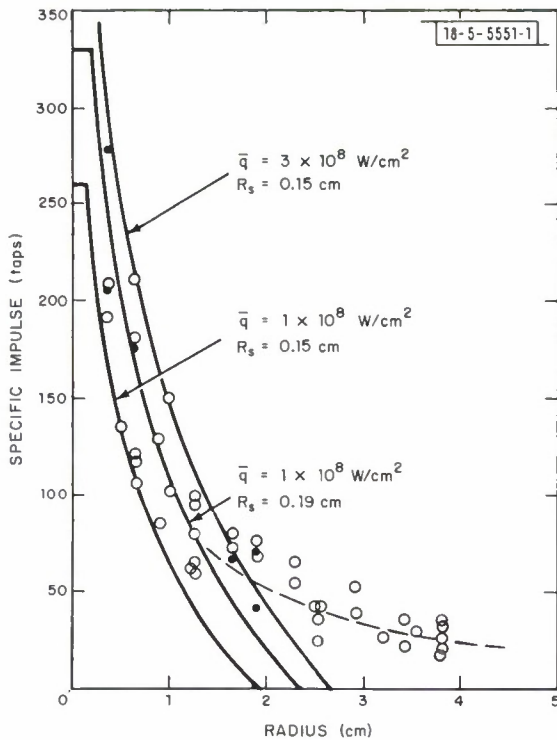


Fig. I-17. Radial specific impulse distribution. The measurements were taken from single shots with average power densities between 1 and 2×10^8 W/cm². The open symbols are integrated pressure measurements and the solid symbols are pendulum measurements. The solid lines were calculated with the use of Eq. (I-2).

The experiments consisted of irradiating the pendulum directly with both single- and double-pulse shots to measure the focal-spot impulse with the pendulum and the radial peak pressure and impulse distributions with the pressure gauges. Points away from the pendulum were also irradiated so as to check the specific impulse obtained by integrating the pressure-gauge readings against the pendulum measurements.

b. Experimental Results

Previous theoretical and experimental work¹⁵⁻²³ has dealt with impulsive coupling to targets in air with irradiation by a high-power CO₂ laser pulse and the attendant formation of a laser-supported detonation (LSD) wave. Here we present a detailed comparison of experimental measurements and predictions from the simple cylindrical blast-wave model. This model, which is described in detail in Ref. 20, yields the following expression for the specific impulse delivered to a target;

$$I_s = P_s \tau_p \left[1 + \ln \frac{P_s}{P_o} \right] \quad . \quad (I-1)$$

Here P_s is the pressure in the focal spot, τ_p is the laser pulse length, and P_o is the ambient gas pressure. The peak focal-spot pressure developed in ambient air is given approximately by^{20,21}

$$P_s \approx 7 \times 10^{-4} (\bar{q})^{2/3} \quad ,$$

where the average power density (\bar{q}) is in W/cm² and the pressure is in bars. Maximum impulse delivery is predicted to occur when the laser pulse length is equal to the time it takes the LSD wave to propagate one focal-spot diameter. The specific impulse distribution outside the focal spot is given by^{22,23}

$$I(R) = P_s \tau_p \ln \left[\frac{P_s}{P_o} \left(\frac{R_s}{R} \right)^2 \right] \quad , \quad (I-2)$$

where R_s is the focal-spot radius and $R > R_s$.

In Fig. I-16, a comparison between measured and predicted focal-spot specific impulse for single pulses is shown for two focal-spot sizes. The measured impulse was normalized by the target area (0.11 cm²) to give an average specific impulse in the focal spot. With the 30-m focusing mirror, the half-power focal-spot diameter was about 0.29 cm and for the 50-m mirror it was about 0.46 cm. The dashed line was fit to the data with a slope of 1/3 while the solid line was calculated with the use of Eq. (I-1). The theory predicts a slope slightly greater than the slope of 1/3 shown by the data in Fig. I-16.

A comparison of predicted and measured radial specific impulse distribution outside the focal spot for single pulses is presented in Fig. I-17. These data were all measured for shots on which the average power density was between 1 and 2×10^8 W/cm². The open symbols are integrated pressure-gauge measurements and the solid symbols refer to pendulum measurements. The solid lines were calculated with the use of Eq. (I-2) for the indicated values of power density and focal-spot radius to show the sensitivity of the results to these parameters. The dashed line shows the trend of the measurements at large radii where the strong shock approximation used in the cylindrical blast-wave model breaks down.

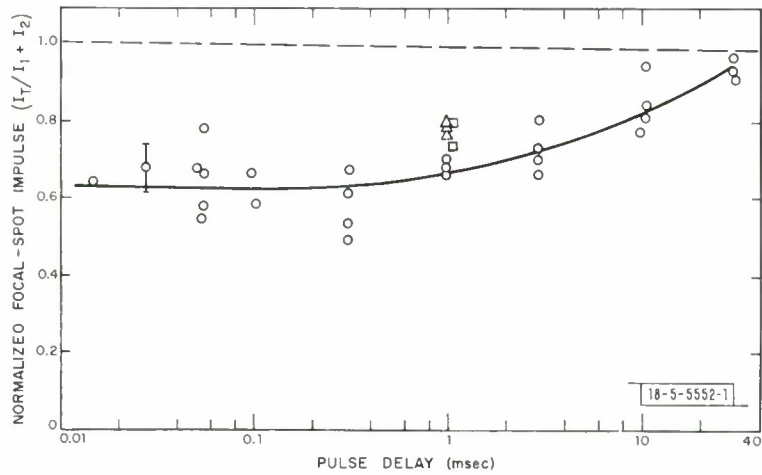


Fig. I-18. Normalized focal-spot impulse as a function of delay time. The solid line shows the trend of the data. The circles indicate the shots where the two pulses had about the same energy ($E_1 \approx E_2$). The triangles indicate shots where $E_1 \approx 3E_2$ and the squares indicate shots where $E_1 \approx 1/3E_2$.

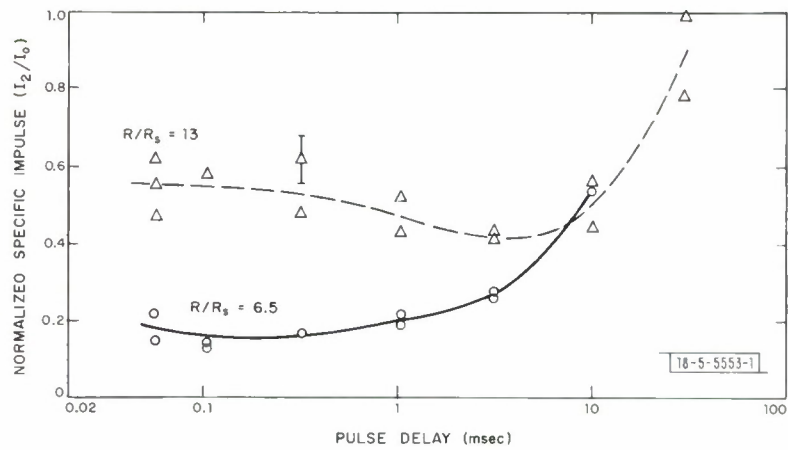


Fig. I-19. Normalized specific impulse at two radial positions. Here I_0 is the impulse which would have been delivered by pulse 2 in the absence of pulse 1. The focal-spot radius (R_s) is 0.19 cm.

The results shown in Figs. I-16 and -17 indicate the cylindrical blast-wave model yields results which are in fair agreement with the measurements.

Results for the double-pulse shots are shown in Fig. I-18 where the normalized focal-spot impulse is plotted as a function of the pulse delay time. The normalized impulse is the total measured impulse divided by the sum of the impulse which would have been delivered by pulses 1 and 2 if they were fired individually. The circles indicate shots where the two pulses had about the same energy ($E_1 \approx E_2$). The triangles indicate shots where $E_1 \approx 3E_2$ and the squares indicate shots where $E_1 \approx 1/3E_2$. These data indicate a short delay asymptote of roughly 0.63 and an increase to unity at a pulse delay of 30 msec. Observations of the dynamics of the plasma generated by the second pulse with a high-speed streak camera typically showed simultaneous plasma initiation at multiple points in the focal volume. In some cases, the initiation of a plasma wave which rapidly moved away from the target in the low-density gas left by the first pulse was observed. Interferometric observations¹⁴ indicate the residual gas density at 10- to 100- μ sec delays is on the order of 0.2 amagat or less. The phenomenon of multiple breakdowns in the focal volume was observed for pulse delays of up to 10 msec and is believed to be caused by particulate matter generated by irradiation of the target by the first pulse.¹⁴ In all cases, smoothly developing LSD waves initiated at the target surface were observed during irradiation by the first pulse. The effect of multiple-breakdown initiation sites in the focal volume is to cause volume absorption of the laser energy away from the target surface and, hence, yield lower pressure and impulse at the target. Similar laser-target decoupling was observed when a plasma wave was launched in the low-density gas left by the first pulse. This is explained by the fact that the cylindrical blast-wave model predicts the peak specific impulse is roughly proportional to the initial gas density to the 2/3 power. The data (1-msec pulse delay) for shots with proportionately more energy in the first or second pulse show a slight increase in the total impulse transferred. This indicates that in the limit, one pulse will dominate and the resulting impulse will approach the single-shot limit. The data show a fair amount of scatter which is caused by the variability of the multiple-breakdown process during the second pulse.

The data presented in Fig. I-19 show the effect of the first pulse on the specific impulse at two radial positions outside the focal spot. Here I_0 is the impulse which the second pulse would have delivered in the absence of the first pulse. These results show the volume disposition of energy during the first pulse reduces the specific impulse to about 20 percent of its normal value at $R/R_s = 6.5$, while at twice that radius it is only reduced to about 50 percent of its normal value. Typical pressure pulses at a radius of 1.27 cm ($R/R_s \approx 6.5$) are shown in Figs. I-20 and -21 for pulse delays of 100 μ sec and 3.1 msec, respectively. For a 100- μ sec delay the second pressure pulse is much reduced, while for the 3.1-msec delay it is only slightly reduced. The energy of the first pulse in Fig. I-21 was somewhat smaller than that of the second pulse and so the pressure due to the first pulse was reduced.

c. Conclusions

The single-pulse results presented here show that the cylindrical blast-wave model adequately describes the gross features of momentum transfer to targets in the event laser-supported detonation waves are initiated, and we conclude this model may be used to correlate data taken under quite different experimental conditions.

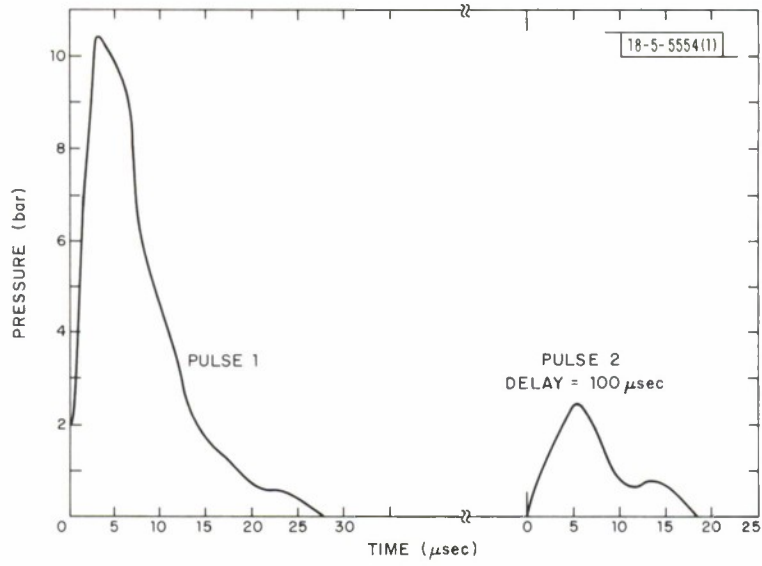


Fig. I-20. Pressure history at $R = 1.27$ cm ($R/R_S = 6.5$) for the initial pulse and a pulse delayed by 100 μ sec. Here $\bar{q}_1 \approx 1.5 \times 10^8$ W/cm² and $\bar{q} \approx 2.7 \times 10^8$ W/cm².

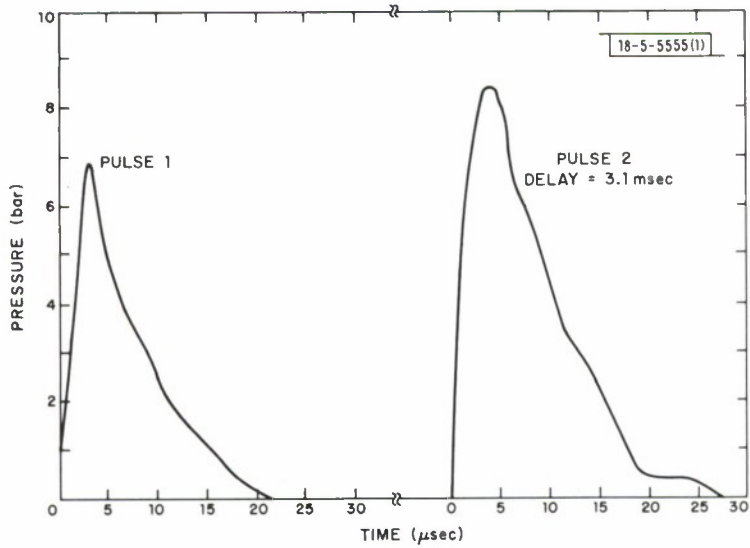


Fig. I-21. Pressure history at $R = 1.27$ cm ($R/R_S = 6.5$) for the initial pulse and a pulse delayed by 3.1 msec. Here $\bar{q}_1 \approx 6.7 \times 10^7$ W/cm² and $\bar{q}_2 = 4 \times 10^8$ W/cm².

The double-pulse results indicate that for pulses with power densities on the order of 10^8 W/cm^2 and a gain-switched leading edge spike, there is no impulse coupling enhancement window as was reported in Ref. 24 for different experimental conditions. The impulse and pressure delivered by the second pulse are effectively decoupled from the focal-spot region for about the time required for the disturbance created by the first pulse to relax to near ambient conditions. Thus, the time required for independent impulse delivery by pulses in a pulse train is concluded to be roughly the time it takes to clear the focal volume when there is crossflow of air across the focal spot.

J. E. Lowder R. W. O'Neil
H. Kleiman L. C. Pettingill

3. Ballistic Pendulum for High-Power Laser Measurements

An experimental, cavity type, ballistic pendulum was fabricated and is presently undergoing testing [see Fig. I-22(a)]. This pendulum is intended to be a prototype of a much heavier instrument which will be used in the diagnostics and measurements of high-power laser beams.

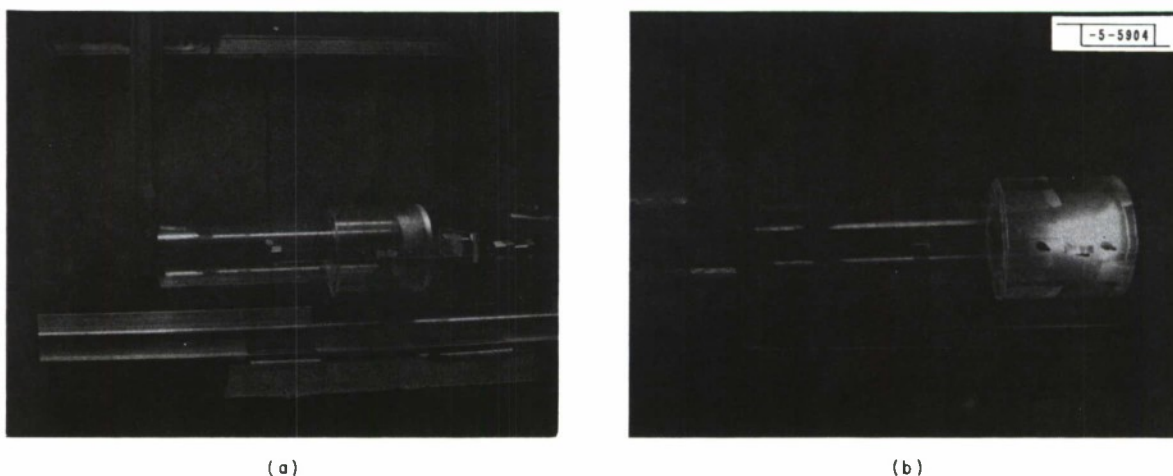


Fig. I-22. (a) Experimental ballistic pendulum; (b) experimental pendulum with plasma after exposure to laser beam.

The pendulum will be constructed such that the momentum transferred to it by the laser beam and, hence, the deflection will be proportional to the laser energy. This can be ensured by designing the pendulum cavity so that the expansion of the blast wave generated at the target surface is effectively one-dimensional. The design of the prototype pendulum permits easy removal and insertion of cavities of different dimensions as well as target plates. The pendulum is suspended on three cables 123 cm long. The deflection of the pendulum is viewed with a TV camera and the readings can be seen on a TV monitor and/or recorded on magnetic tape. The pendulum and the cavities are made of Plexiglas because its transparency permits direct observation and recording of the plasma luminosity which occurs during interaction of the laser beam with the target [see Fig. I-22(b)]. The evaluation of the pendulum includes the measurements of the impulse (I) as a function of:

- (a) Shape of the cavity
- (b) Length of the cavity
- (c) Diameter of the cavity

- (d) Target material (aluminum, graphite)
- (e) Laser beam energy (see graph, Fig. I-23).

After proper calibration, the final version of the pendulum will be used as a sensitive, energy-measuring device for high-energy laser beams, coupling coefficients, and losses in beam energy due to air breakdown.

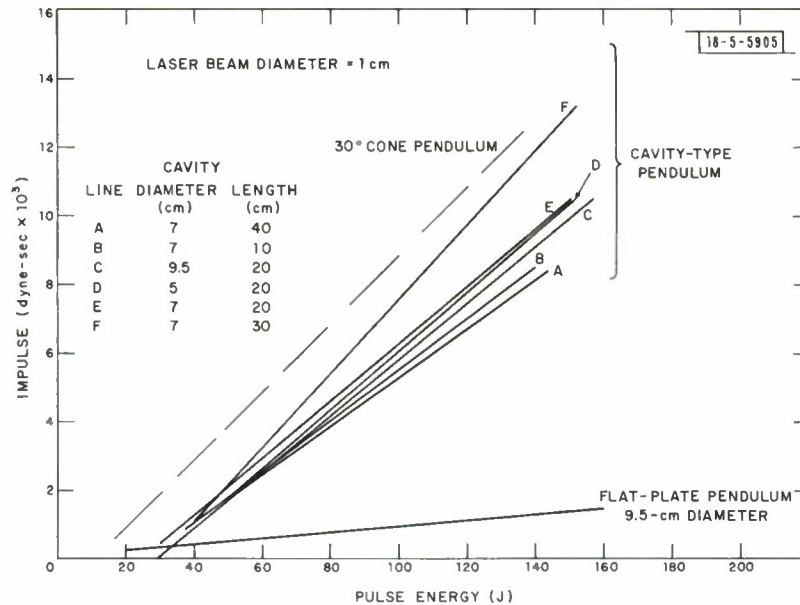


Fig. I-23. Total impulse transferred to ballistic pendulum as a function of laser beam energy.

A chamber 20 m long and 0.6×0.6 m in cross section is now under construction. The chamber consists of seven separate sections and has two of its sides made of Plexiglas. The chamber will be used in conjunction with the ballistic pendulum in evaluation of high-energy laser beams. The purity of the air inside the chamber will be controlled by three filter-equipped fans.

J. Rotstein S. Marcus
D. E. Lencioni J. R. Bielinski

4. Laser Heating of Metallic Surfaces

The instantaneous front surface heating rate of metallic surfaces may be determined by measuring the front surface temperature history and then calculating the heating rate with the relation²⁵

$$F(0, t) = \frac{K}{\sqrt{\pi k}} \int_0^t \frac{\frac{dT}{dt'}}{\sqrt{t-t'}} T(0, t') dt'$$

where F is the heating rate, K is the thermal conductivity, k is the thermal diffusivity, and T is the temperature. A computer program has been written which evaluates this equation and is described in detail below. In addition, the results of an experimental program to measure the surface temperature history of a copper target irradiated by a pulsed $10.6\text{-}\mu\text{m}$ laser are

presented. The surface temperature history was measured with thin-film copper-constantan thermocouples which had response times on the order of a few microseconds. Surface temperature histories were measured in both the presence and absence of plasma at the target surface. Surface heating rates were determined for these cases and this allowed the surface absorptivity to be determined as a function of time.

a. Theoretical Development

Thermal response to an incident pulse depends markedly on the thermocouple junction depth below the surface. As the junction depth is increased, the diffusion of heat laterally in the surface layer becomes important. A computer code has been generated to solve the time-dependent heat-flow equation in the case of axial symmetry about the thermocouple. For thermocouples with surface layers less than 10 μm thick, the results indicate that an infinite copper-constantan thermocouple (i.e., a thin copper layer over a semi-infinite constantan slab) is a reasonable model.

b. Surface Thermocouples

A thermocouple with a copper surface layer thickness less than 1 μm can be analyzed by assuming that the thermal properties are essentially those of a semi-infinite block of constantan. For such a case, the temperature change T and the absorbed flux F are related by the following equations²⁵

$$\begin{aligned} T(0, t) &= \sqrt{\frac{k}{\pi}} \frac{1}{K} \int_0^t \frac{F(0, t') dt'}{\sqrt{t - t'}} \\ F(0, t) &= \frac{K}{\sqrt{\pi k}} \int_0^t \frac{\frac{d}{dt'} T(0, t') dt'}{\sqrt{t - t'}} \end{aligned} \quad (I-3)$$

where the thermal properties are those of constantan.

The most straightforward procedure is to use Eq. (I-3) and expand T in some basis set. A linear spline expansion is used here

$$T(0, t) = \sum T_i W_i(t) \quad .$$

Here the spline function is defined by

$$W_i(t) = \begin{cases} \frac{t - t_{i-1}}{t_i - t_{i-1}} & t_{i-1} < t < t_i \\ \frac{t_{i+1} - t}{t_{i+1} - t_i} & t_i < t < t_{i+1} \end{cases} \quad .$$

The resulting finite difference equations are given by

$$\begin{aligned} F_j &= \frac{K}{\sqrt{k\pi}} \sum_{i=2}^j \frac{T_i - T_{i-1}}{t_i - t_{i-1}} 2(\sqrt{t_j - t_i} - \sqrt{t_j - t_{i-1}}) \\ T_i &= \sqrt{\frac{k}{\pi}} \frac{1}{K} \sum_{j=2}^i \frac{F_j - F_{j-1}}{t_j - t_{j-1}} \frac{2}{3} \begin{bmatrix} 2(t_i - t_{j-1}) \sqrt{t_i - t_{j-1}} \\ -2(t_i - t_j) \sqrt{t_i - t_j} \end{bmatrix} \end{aligned} \quad (I-4)$$

These equations have been used with limited success to determine F . The basic problem with this approach is the numerical derivative which appears. By integrating Eq. (I-4) by parts, an alternative starting point is given by

$$F(0, t) = \frac{K}{\sqrt{\pi k}} \left[\frac{T(0, t)}{\sqrt{t}} + \frac{1}{2} \int_0^t \frac{T(0, t) - T(0, t')}{(t - t')^{3/2}} dt' \right] .$$

The numerical derivative is still present implicitly in the second term, however, and the numerical procedure still amplifies small random errors incurred by digitizing the experimental temperature points T_i . This is a general problem for inversions where the integrand is generated by experimental data. A root-mean-square fit to the temperature also can be used. Because of the presence of a cusp in the thermocouple response, a fit in the range $t < t_p$ and a second in the range $t > t_p$ are the most reasonable choices. A second alternative is to expand the pulse in a polynomial expansion in the same way and adjust the coefficients with a rms fit of the experimental temperature points.

c. Polynomial Approximation of $F(t)$

From the previous section there are two equations which can be used to determine the absorbed flux. Because of the difficulties associated with numerical derivatives of the temperature, the equation which defines the junction temperature in terms of the surface flux will be the starting point. The flux will be expanded in a polynomial over two ranges; the first from zero to the time associated with the peak temperature and the second from the peak to the maximum time recorded.

$$F(t) = \begin{cases} \sum C_n t^n & 0 < t < t_p \\ \sum C'_n t^n & t_p < t < t_m \end{cases} .$$

For times less than t_p the temperature is given by

$$\begin{aligned} T &= \sqrt{\frac{k}{\pi}} \frac{1}{K} \sum C_n \int_0^t \frac{t'^n dt'}{\sqrt{t - t'}} \\ &\equiv \sum C_n L_n(t) . \end{aligned}$$

The evaluation of the integrals is accomplished by an 8th-order Gauss-Jacobi quadrature.

$$\int_0^1 \frac{g(x)}{x^{1/2}} dx = \sum_{i=1}^8 f(x_i) W_i$$

This procedure will integrate a 15th-order polynomial exactly and the values of x_i and W_i are given in Ref. 26.

The root-mean-square fit of the temperature is given by minimizing the variation of the mean-square deviation as follows

$$\frac{\delta}{\delta C_n} \sum_{i=1}^N [T_i - T(t_i)]^2 = 0 ,$$

where T_i is the temperature at time t_i obtained by digitizing the recorded temperature histories and N is the number of measurements made before the end of the pulse.

For most reasonable pulses with a thin surface layer, a 4th-order polynomial is sufficient to describe $F(t)$. For thicker layers, higher-order integration schemes are needed to take into account the rapid change in $K(\beta/t - t')$ at $t \rightarrow t'$.

For times greater than t_p , the temperature contribution due to flux absorbed before t_p is given by

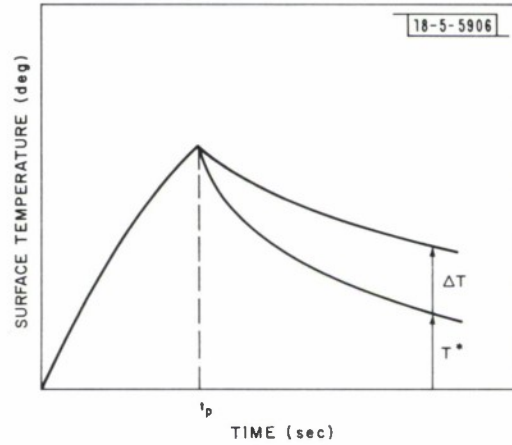
$$T^*(t) = \sqrt{\frac{k}{\pi}} \frac{1}{K} \sum C_n \int_{t_p}^t \frac{t'^n}{(t-t')^{1/2}} dt' .$$

If there is flux absorption after t_p , this term is only a partial contribution to the temperature. The remaining part or residual temperature increase is given by

$$\begin{aligned} \Delta T(t) &= \sqrt{\frac{k}{\pi}} \frac{1}{K} \int_{t_p}^t \sum \frac{C'_n t'^n dt'}{\sqrt{t-t'}} \\ &= \sum C'_n L'_n(t) . \end{aligned}$$

This situation is illustrated in Fig. I-24. The values of C'_n are determined by the same procedure used to determine the values of C_n .

Fig. I-24. Illustration of the temperature (T^*) due to heating prior to time t_p and the contribution ΔT due to heating after time t_p .



d. Arbitrary Junction Depth

For a semi-infinite thermocouple composed of a layer of copper of thickness l and a semi-infinite constantan substrate, the time dependence of the temperature in the solid due to an arbitrary absorbed flux $F(-l, t)$ is governed by the following equations.

$$\frac{\partial^2 T}{\partial z^2} - \frac{1}{k'} \frac{\partial T}{\partial t} = 0 \quad -l < z \leq 0$$

$$\frac{\partial^2 T}{\partial z^2} - \frac{1}{k} \frac{\partial T}{\partial t} = 0 \quad 0 < z .$$

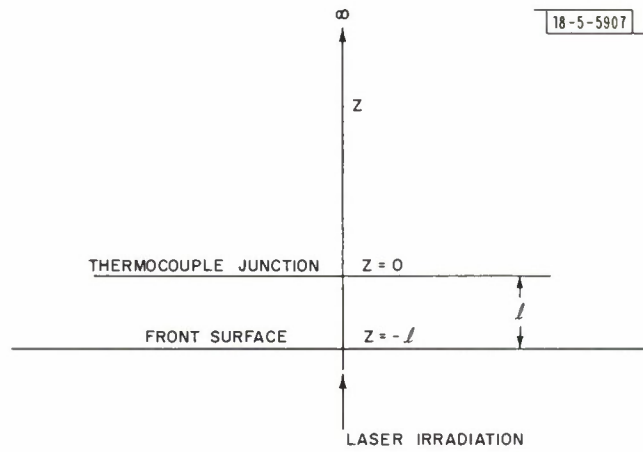


Fig. I-25. Coordinate system for subsurface thermocouple junctions.

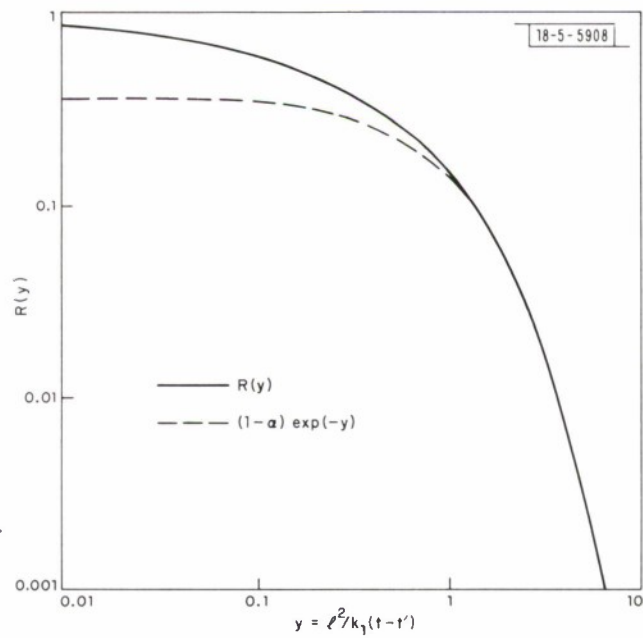


Fig. I-26. The "depth function" $R(y)$ for subsurface thermocouple junctions.

The coordinate system is illustrated in Fig.I-25. The boundary conditions are as follows.

$$K' \left. \frac{\delta T}{\delta z} \right|_{-l} = F(-l, t)$$

$$K' \left. \frac{\delta T}{\delta z} \right|_{-0} = K \left. \frac{\delta T}{\delta z} \right|_{+0}$$

$$T(\rightarrow \infty) = 0$$

Here K and k are the thermal conductivity and thermal diffusivity of the substrate. A similar definition applies to the primed values for the surface layer.

The Laplace transform of T is designated by ν and at the junction (i.e., $z = 0$) the value of ν is determined by the usual procedure of matching boundary conditions.²⁷ Since only the temperature at $z = 0$ and the absorbed flux at $z = -l$ are of interest in the following discussion, the z dependence will be implicitly understood. The resulting expression for ν is given by

$$\nu(s) = f(s) [Kq \cosh(q'l) + K'q' \sinh(q'l)]^{-1}$$

Here $q = \sqrt{s/k}$, similarly for q' , and $f(s)$ is the Laplace transform of the absorbed flux. This may be rearranged by expanding the hyperbolic functions

$$\nu(s) = 2f(s) \sqrt{\frac{k}{SK^2}} \frac{1}{1+\sigma} \sum_{n=0}^{\infty} \alpha^n e^{-(2n+1)lq'}$$

Here $\sigma = (K/K') \sqrt{k'/k}$ and $\alpha = (\sigma - 1)/(\sigma + 1)$.

The temperature at the junction is given by the inverse Laplace transform of $\nu(s)$

$$T(t) = \sqrt{\frac{k}{\pi}} \frac{1}{K} \int_0^t \frac{F(t')}{(t-t')^{1/2}} R[l^2/4k'(t-t')] dt'$$

where

$$R(y) = (1 - \alpha) \sum_{n=0}^{\infty} \alpha^n e^{-(2n+1)^2 y}$$

A plot of R is shown in Fig.I-26.

For completeness, the absorbed flux as a function of junction temperature is also given by

$$F(t) = K \sqrt{\frac{1}{\pi k}} \int_0^t \frac{dT(t')}{dt'} \frac{e^{-b/(t-t')}}{(t-t')^{1/2}} dt'$$

where $b = l^2/4k'$.

e. Experimental Results

Thin-film copper-constantan thermocouples mounted in a copper block²⁸ were irradiated with 10.6- μ m laser pulses with average incident intensities which varied from 8×10^4 to 5×10^6 W/cm². Three measurements are reported here for the case of (1) low power density (8×10^4 W/cm²), (2) intermediate power density near the breakdown threshold (3×10^5 W/cm²), and (3) a high power density (5×10^6 W/cm²). The pulse lengths ranged from 18 to 32 μ sec in duration with no visible breakdown plasma observed for cases (1) and (2). Case (3) was above the

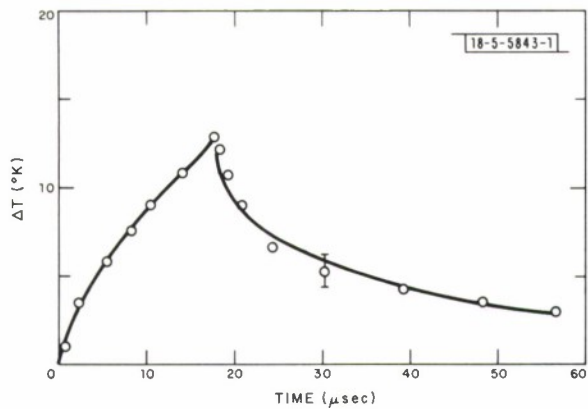


Fig. I-27. Surface temperature history for case (1); average incident power density of 8.3×10^4 W/cm² with no visible surface plasma.

Fig. I-28. Surface temperature history for case (2); average incident power density of 3×10^5 W/cm² with no visible surface plasma.

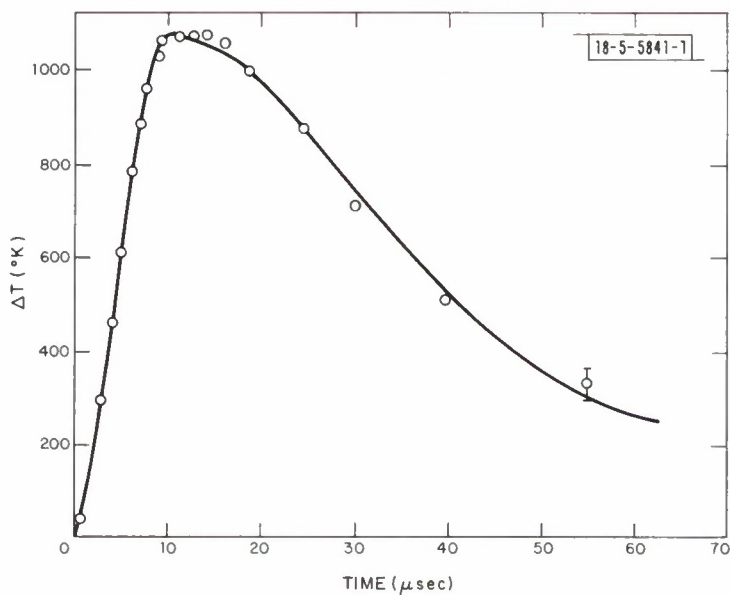
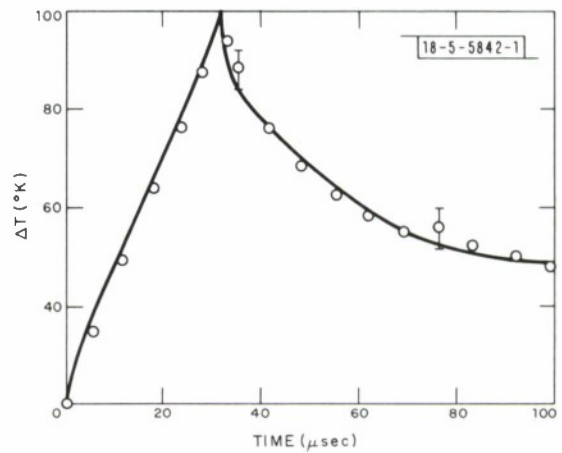


Fig. I-29. Surface temperature history for case (3); average incident power density of 5×10^6 W/cm² with a strong surface plasma initiated immediately.

breakdown threshold and a bright surface plasma was initiated within a few hundred nanoseconds of the initiation of the laser pulse.

The CO₂ laser²⁹ used produced a pulse of variable length and nominally a square wave or a ramp with a 200- to 300-nsec leading edge spike which had an intensity of from 1.5 to 2 times the average. The half-power focal-spot diameter was approximately 0.2 cm for these experiments.

The measured surface temperature histories for cases (1), (2), and (3) are shown in Figs. I-27, -28, and -29. The data points were digitized from polaroid photographs and the measurement uncertainty is indicated by the error bars. The solid lines are the polynomial curve fits generated by the computer program described previously. The sharp cusps evident in the surface temperature responses shown in Figs. I-27 and -28 occur at the end of the incident laser pulse. For case (3) shown in Fig. I-29 where a surface plasma was generated, there was no evidence of a sharp surface heating rate cutoff.

The temperature histories were used to determine the surface heating rates for cases (1), (2), and (3) shown in Figs. I-30, -31, and -32. For cases (1) and (2), there is a sharp cutoff in heating rate at the end of the laser pulse, although the heating rate does not drop to near zero for case (2). The reason for this is not known since there was no visible plasma layer present. The heating rate for case (3) is shown in Fig. I-32. Here the heating rate peaks and then decreases while the laser pulse is on. This is caused by the plasma absorbing the laser radiation and decoupling from the target surface as the laser-supported-absorption wave propagates away from the target.

The surface heating rate histories and the measured incident laser power densities were used to determine the variation of the surface absorption coefficient during the laser pulse. The absorption coefficients for three cases are shown in Fig. I-33 as functions of time normalized by the individual pulse lengths. For the case of no visible plasma, the absorption coefficient varies from 1 to 4 percent, while for the case of a strong surface plasma, the absorption coefficient rapidly peaks to a value over 7 percent and decreases during the laser pulse.

The results indicate that the transfer of energy to metallic surfaces with 10.6- μ m laser irradiation can be increased if a surface plasma is generated and the laser pulse is short so as not to allow the plasma to propagate very far from the surface.

J. E. Lowder
D. L. Mooney
R. W. O'Neil

5. Plasma Enhancement of Thermal Coupling to Targets

During this period, experiments were performed to determine the effect of plasma formation on the thermal coupling of 10.6- μ m laser pulses to metallic targets, specifically to copper and aluminum. The targets incorporated the fast-response surface thermocouples described in the previous Optics Research Report.¹ In order to measure surface temperature changes outside the focal spot, a linear array of five thermocouples was used, each thermocouple separated by 3.2 mm. We can thus report here the first temperature measurements of laser-pulse-bombarded target surfaces which are both spatially and temporally resolved.

The experimental layout for our thermal-coupling measurements is shown schematically in Fig. I-34. The pulsed, electron-beam laser is capable of producing approximately 5 J in 10- to 100- μ sec pulses. After passing through a KCl beam-splitting wedge, used to monitor the pulse shape and energy, the beam is focused onto the middle thermocouple of the target.

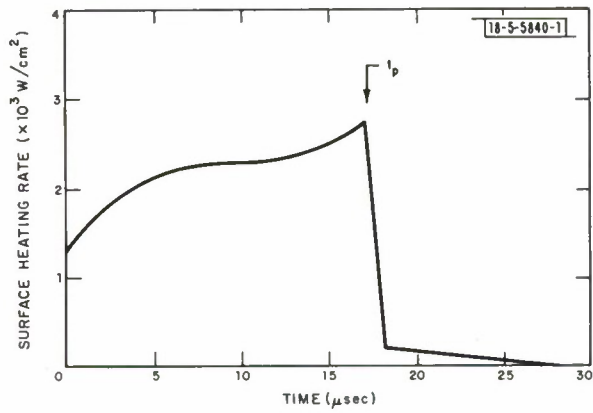


Fig. I-30. Surface heating rate for case (1); average absorption coefficient was 2.7 percent.

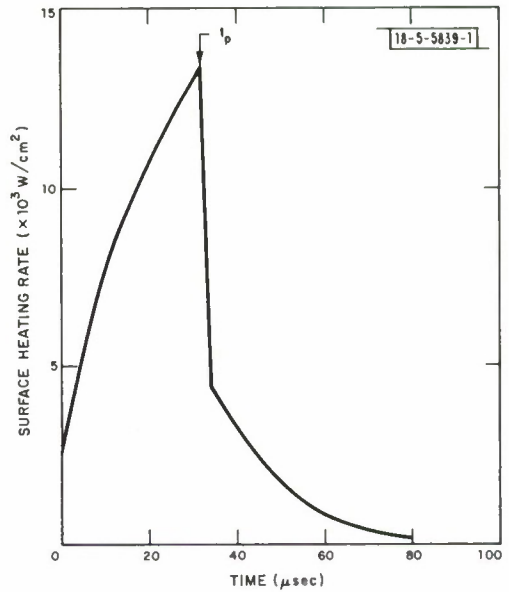


Fig. I-31. Surface heating rate for case (2); average absorption coefficient was 3 percent.

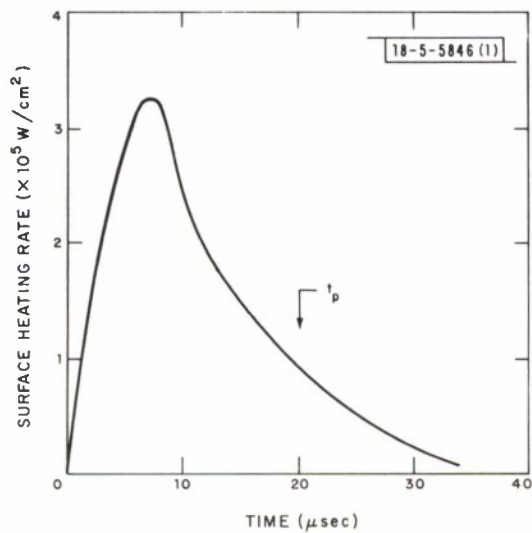


Fig. I-32. Surface heating rate for case (3); average absorption coefficient was 4.2 percent.

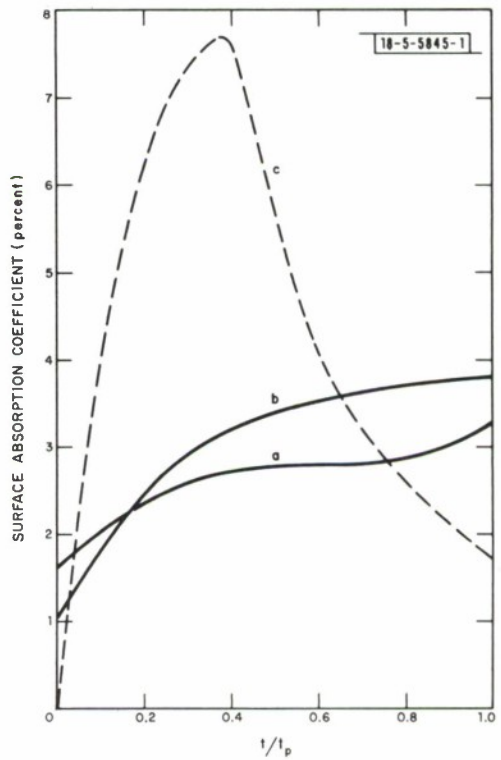


Fig. I-33. Surface absorption coefficients for cases (1), (2), and (3) as functions of time normalized by the pulse lengths.

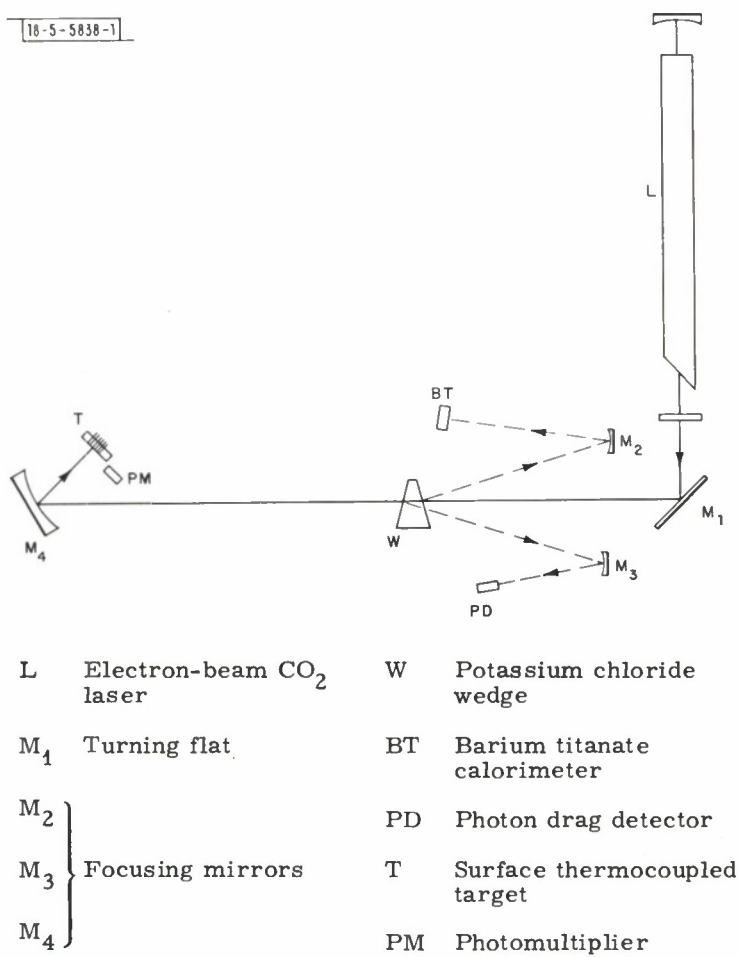


Fig. I-34. Experimental layout for thermal-coupling measurements.

A photomultiplier, viewing parallel to the target surface, detects plasma luminosity. Preliminary to the experiments, the focused spot size is measured by discoloring heat-sensitive paper at various levels of beam attenuation.

The thermal coupling with no detectable plasma formation at the target surface was first measured by attenuating the incident laser intensity to less than 10^5 W/cm^2 . Under these conditions, a temperature increase was registered on the middle thermocouple only. Upon increasing the laser intensity to the point where surface-induced breakdown occurred, temperature increases were sensed by all five thermocouples. Figure I-35 shows the thermocouple responses for a typical shot, with breakdown, on a copper target. Also shown in Fig. I-35 is a plot of distance from the middle thermocouple vs arrival time of the thermal disturbance. It can be seen from this figure that the disturbance spreads outward at supersonic velocities typical of blast-wave expansion, much too fast to be due to surface conduction. The observed time delay also indicates that the plasma heating of the target is predominantly due to electronic conduction or short-range radiative transfer.

The procedure for extracting the absorbed flux as a function of time from the observed thermocouple responses is described elsewhere in this Optics Research Report (Sec. I-B-4). A typical example of the results of such an inversion for one of the shots on aluminum is shown in Fig. I-36. The absorbed flux at each thermocouple is then integrated in time to give a radial profile of the absorbed energy fluence. This profile, which can be fit to an exponential, is in turn integrated spatially to give the total absorbed laser energy. In the case where no plasma is generated, the absorbed energy is simply the product of absorbed fluence and the measured focal-spot area. In each case, the thermal-coupling coefficient is defined as the ratio of absorbed to incident laser energy.

TABLE I-1 MEASURED PLASMA ENHANCEMENT OF THERMAL COUPLING		
Surface	Coupling Coefficients	
	Low Intensity	With Breakdown
Aluminum	0.039	0.27
Copper	0.036	0.33

The coupling coefficients thus determined for copper and aluminum are shown in Table I-1. It is seen that for both these metals, there is a large coupling enhancement when laser-induced breakdown occurs. This phenomenon, arising from the inverse bremsstrahlung in the plasma and subsequent transfer to the target, also was observed recently by Rudder.³⁰ He deduced this enhancement from his measurements of the total temperature increase due to a train of CO_2 laser pulses. No spatial or resolved temporal dependence of the energy absorption is obtained with his technique.

In the next period, we hope to extend our technique to the case of large spot sizes, using one of our 500-J lasers with a stable resonator.

S. Marcus
S. Manlief
D. L. Mooney

C. STABLE CO₂ LASER MEASUREMENTS

We have made several major improvements in the experimental setup used to determine CO₂ isotope laser frequencies.

The first improvement relates to the long-term stabilization of CO₂ lasers by means of the 4.3- μ m fluorescence technique. We have designed, tested, and built new, low-pressure CO₂ stabilization cells external to the lasers in which significantly larger signal collection efficiency was achieved simultaneously with a great reduction in background radiation, which was the primary limit in high-quality InSb photovoltaic detectors.

Also, we have evaluated and tested several large area InSb detectors and determined that LN₂ cooled background greatly diminished 1/f noise in addition to the expected reduction in the white noise due to the lower temperature background radiation.

In the new design, the low pressure gas cell, the LN₂ cooled radiation collector, and the IR detector are all integral parts of one evacuated housing assembly which also minimizes signal absorption by windows and eliminates all other sources of absorption. Because of the vacuum enclosure, diffusion of other gases into the low-pressure gas reference cell is almost completely eliminated; therefore, the time period available to use a reference gas cell has greatly increased and considerably less time has to be wasted on repumping and refilling procedures.

In addition to greatly improved reliability and maintenance, the new stabilizing cells will result in S/N improvements between 1 and 3 orders of magnitude. The exact amount will be determined by the quality and area of 2 new detectors to be purchased in the near future.

We have designed and built a new LN₂ dewar which will enable us to more effectively use high-speed HgCdTe varactor photodiodes. We expect to extend the usable beat frequency range well beyond 100 GHz.

We have specially designed and built a new laser and associated trapping equipment which will enable us to test ¹⁴CO₂ isotopes.

We are in the process of interfacing a Data General Nova II mini-computer with our present experimental setup, in order to speed up and simultaneously improve the accuracy of our experimental procedure to determine isotope laser frequencies. The new setup will also enable us to determine on line many other parameters such as vibrational-rotational constants and combination frequencies.

C. Freed

REFERENCES

1. Optics Research Report, Lincoln Laboratory, M.I.T. (1974:1), p. 4, DDC AD-A001971.
2. Optics Research Report, Lincoln Laboratory, M.I.T. (1973:2), p. 7, DDC AD-779917/4.
3. R. W. O'Neil, H. Kleiman, and J. E. Lowder, Appl. Phys. Lett. 24, 118 (1974).
4. R. W. O'Neil, H. Kleiman, L. C. Marquet, C. W. Kilcline, and D. Northram, Appl. Opt. 13, 314 (1974).
5. D. W. Gregg and S. J. Thomas, J. Appl. Phys. 37, 2787 (1966).
6. C. H. Skeen and C. M. York, Appl. Phys. Lett. 12, 369 (1968).

7. E. D. Jones and R. R. Rudder, Proceedings of the Underground Nuclear Test Measurements Symposium I, No. DNA 2894P1 (1972).
8. S. A. Metz, Appl. Phys. Lett. 22, 241 (1973).
9. J. E. Lowder and L. C. Pettingill, Appl. Phys. Lett. 24, 204 (1974).
10. C. T. Walters and R. H. Barnes, "An Investigation of Mechanisms of Initiation of Laser Supported Absorption (LSA) Waves," Semiannual Report, ARPA Order 2413, Battelle Columbus Laboratories (1973).
11. R. B. Hall, W. E. Maher, and P. S. P. Wei, "An Investigation of Laser Supported Detonation Waves," AFWL-TR-73-28 (June 1973).
12. R. R. Rudder, "Momentum Transfer to Solid Target Discs by Pulsed One-Micron Radiation," Air Force Weapons Laboratory Laser Digest, AFWL-TR-73-273 (December 1973), p. 137.
13. J. F. Ready, Effect High-Power Laser Radiation (Academic Press, New York, 1971), p. 96.
14. Optics Research Report, Lincoln Laboratory, M.I.T. (1973:2), pp. 29-43, DDC AD-779917/4; (1974:1), pp. 9-11, DDC AD-A001971.
15. J. E. Lowder and L. C. Pettingill, DoD Laser Effects/Hardening Conf., Monterey, California, 23-26 October 1973.
16. G. H. Canavan, P. E. Nielsen, and R. D. Harris, Air Force Weapons Laboratory Laser Division Digest LRD-72-1 (June 1972), p. 127.
17. A. N. Pirri, R. Schlier, and D. Northram, Appl. Phys. Lett. 21, 79 (1972).
18. J. E. Lowder, D. E. Lencioni, T. W. Hilton, and R. J. Hull, J. Appl. Phys. 44, 2759 (1973).
19. L. R. Hettche, J. T. Schriempf, and R. L. Stegman, J. Appl. Phys. 44, 4079 (1973).
20. A. N. Pirri, Physics of Fluids 16, 1435 (1973).
21. J. E. Lowder and L. C. Pettingill, Joint Strategic Sciences Meeting, San Diego, California, 7-9 January 1974.
22. A. N. Pirri, DoD Laser Effects/Hardening Conf., Monterey, California, 23-26 October 1973.
23. P. E. Nielsen, DoD Laser Effects/Hardening Conf., Monterey, California, 23-26 October 1973.
24. R. B. Hall, W. E. Maher, and D. F. Nelson, DoD Laser Effects/Hardening Conf., Monterey, California, 23-26 October 1973.
25. C. J. Scott, "Transient Experimental Techniques for Surface Heat Flux Rates," in Measurement Techniques in Heat Transfer, edited by E. R. G. Eckert and R. J. Goldstein (CIRCA Publications, Inc., New York, 1970).
26. H. E. Fettis, Math. Comp. 18, 491 (1964).
27. H. S. Carslaw and J. C. Jaeger, Conduction of Heat in Solids (Clarendon, Oxford, 1959).
28. L. Jones, Medtherm Corporation, Huntsville, Alabama, private communication, November 1973.
29. S. Marcus, Appl. Phys. Lett. 21, 18 (1972).
30. R. R. Rudder, First DoD Conf. on High Energy Laser Technology, San Diego, California, 1-3 October 1974.

II. POLLUTION STUDIES*

A. PARTICIPATION IN THE ST. LOUIS REGIONAL AIR POLLUTION STUDY (RAPS) OF THE U. S. ENVIRONMENTAL PROTECTION AGENCY

In August 1974 our diode laser monitoring van, shown in Fig. II-1, was driven to St. Louis, Missouri for preliminary measurements in conjunction with the U. S. Environmental Protection Agency's first Regional Air Pollution Study. Long path carbon monoxide measurements were performed at three different field sites in the St. Louis area during the two-month period. Ambient CO data were obtained for monitored path length up to 2 km.



Fig. II-1. Diode laser air-monitoring van.

Comparisons were made between laser measurements of ambient CO and those obtained using bag samples which were filled while walking along the laser beam path. Gas chromatography was used to determine the CO concentrations in the bag samples, and several comparisons between these and the laser measurements over a 0.3-km path are listed in Table II-1.

There is generally good correlation between the laser and bag-sample measurements. In fact, total agreement would be expected only if the pollutant concentration was invariant over the entire path.

Figure II-2 shows the CO concentration in St. Louis, as deduced from the first diode laser measurements there. Although the actual monitoring used a 1-sec time constant, this curve was redrawn with an approximately 5-minute time constant to indicate more clearly the trends over the 5-hour period. The CO level rose from 0.5 ppm in mid-afternoon to nearly 2 ppm at the time of peak commuter traffic. A complete report of these St. Louis measurements is in preparation.

R. T. Ku
E. D. Hinkley

* This section describes the work performed at Lincoln Laboratory under the sponsorship of the National Science Foundation (Research Applied to National Needs), with partial support from the U. S. Environmental Protection Agency.

TABLE II-1 COMPARATIVE CO MEASUREMENTS		
Run No.	Laser (ppm)	Bag (ppm)
1	0.55	0.61
2	0.60	0.62
3	0.39	0.56
4	1.65	1.07
5	0.87	1.02
6	3.1	2.3
7	2.13	1.93
8	0.95	0.85

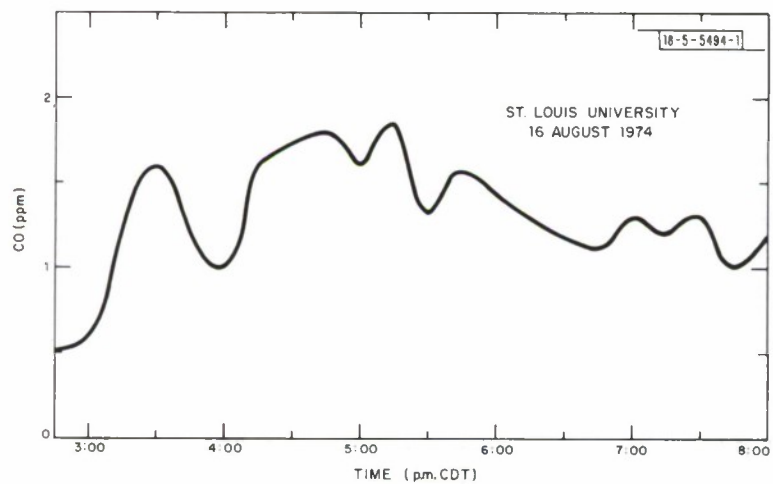


Fig. II-2. Laser monitoring of CO at St. Louis University.
Path length = 0.2 km.

B. DIODE LASER MULTI-POLLUTANT AMBIENT-AIR MONITORING

This work is described in detail in the June 1974 Annual Report to the National Science Foundation (RANN). A summary of this report, having the above title, follows.

Semiconductor diode lasers were constructed and used to study absorption lines of four pollutant gases (CO, NO, O₃, and SO₂) in the 4- to 6- μ m region of the infrared. The high strengths of the CO and NO fundamental bands in this region make it an appropriate one for monitoring at ambient-air sensitivity levels. This was not the case for O₃ and SO₂ whose line strengths in the 4- to 6- μ m region are more than an order-of-magnitude weaker than those at longer wavelengths. Although sufficient sensitivity can be achieved for these two gases in high concentrations near effluent sources, it would be inadequate for ambient-air monitoring. The diode laser was incorporated into a closed-cycle cryogenic cooler, which eliminated the need for liquid helium and made possible long-term monitoring outside the laboratory environment.

Fundamental spectral parameters were obtained by laser spectroscopy for appropriate lines in the 4.7- μ m band of CO and the 5.3- μ m band of NO. Samples of raw automobile exhaust and tobacco smoke showed that any of the strong CO lines could be used for monitoring without substantial interference from other atmospheric gases.

Field measurements were made to determine the beam cross-section characteristics, intensity fluctuations caused by meteorological conditions, and techniques for overcoming such fluctuations. A derivative/ratio technique was used to measure ambient levels of CO to a sensitivity of a few ppb over a 0.61-km atmospheric path. A mobile van, such as shown in Fig. II-1, was purchased and the diode laser system was incorporated into it for CO measurements at other locations - particularly in St. Louis, Missouri, as a part of the Regional Air Pollution Study of the U.S. Environmental Protection Agency. The validity and accuracy of the diode laser system was established over short atmospheric paths of 0.2 and 0.4 km with conventional point-sampling CO instruments. Monitoring of CO over path lengths of 1.5 and 2 km (round-trip) were also performed in the city of St. Louis and at a rural site located across the Mississippi River in Illinois. Preliminary correlations between the measured CO levels and relevant meteorological data are being carried out.

E. D. Hinkley
R. T. Ku

UNCLASSIFIED

SECURITY CLASSIFICATION OF THIS PAGE (When Data Entered)

REPORT DOCUMENTATION PAGE		READ INSTRUCTIONS BEFORE COMPLETING FORM
1. REPORT NUMBER ESD-TR-75-107	2. GOVT ACCESSION NO.	3. RECIPIENT'S CATALOG NUMBER
4. TITLE (and Subtitle) Optics Research		5. TYPE OF REPORT & PERIOD COVERED Semiannual Report 1 July - 31 December 1974
		6. PERFORMING ORG. REPORT NUMBER Optics Research (1974:2)
7. AUTHOR(s) Rediker, Robert H.		8. CONTRACT OR GRANT NUMBER(s) F19628-73-C-0002
9. PERFORMING ORGANIZATION NAME AND ADDRESS Lincoln Laboratory, M.I.T. P.O. Box 73 Lexington, MA 02173		10. PROGRAM ELEMENT, PROJECT, TASK AREA & WORK UNIT NUMBERS ARPA Order 600
11. CONTROLLING OFFICE NAME AND ADDRESS Advanced Research Projects Agency 1400 Wilson Boulevard Arlington, VA 22209		12. REPORT DATE 31 December 1974
		13. NUMBER OF PAGES 48
14. MONITORING AGENCY NAME & ADDRESS (if different from Controlling Office) Electronic Systems Division Hanscom AFB Bedford, MA 01731		15. SECURITY CLASS. (of this report) Unclassified
		15a. DECLASSIFICATION DOWNGRADING SCHEDULE
16. DISTRIBUTION STATEMENT (of this Report) Approved for public release; distribution unlimited.		
17. DISTRIBUTION STATEMENT (of the abstract entered in Block 20, if different from Report)		
18. SUPPLEMENTARY NOTES None		
19. KEY WORDS (Continue on reverse side if necessary and identify by block number)		
optics laser technology thermal blooming	optical devices optical systems	KC-135 laser radar imaging system
20. ABSTRACT (Continue on reverse side if necessary and identify by block number)		
<p>This report covers work of the Optics Division at Lincoln Laboratory for the period 1 July through 31 December 1974. The topics covered are laser technology and propagation and optical measurements and instrumentation.</p> <p>Additional information on the optics program may be found in the ARPA/STO Program Semiannual Technical Summary Reports to the Advanced Research Projects Agency.</p>		

UNCLASSIFIED

SECURITY CLASSIFICATION OF THIS PAGE (When Data Entered)